Master Thesis

Cuprous oxide-based cathodes for photocatalytic water splitting

carried out for the purpose of obtaining the degree of Master of Science (MSc or Dipl.-Ing. or DI)
submitted at TU Wien, Faculty of Technical Chemistry, by

Jana Katharina Kupka

Mat.Nr.: 01446983

under the supervision of
Ao.Univ.Prof. Dipl.-Chem. Dr.rer.nat. Matthias Weil
Institute of Chemical Technologies and Analytics, E164-05

Vienna, November 2021

This work was supported by the AIT Austrian Institute of Technology GmbH under the supervision of Dr. Theodoros Dimopoulos

I confirm, that going to press of this thesis needs the confirmation of the examination committee.

Affidavit

I declare in lieu of oath, that I wrote this thesis and performed the associated research myself, using only literature cited in this volume. If text passages from sources are used literally, they are marked as such.

I confirm that this work is original and has not been submitted elsewhere for any examination, nor is it currently under consideration for a thesis elsewhere.

I acknowledge that the submitted work will be checked electronically-technically using suitable and state-of-the-art means (plagiarism detection software). On the one hand, this ensures that the submitted work was prepared according to the high-quality standards within the applicable rules to ensure good scientific practice "Code of Conduct" at the TU Wien. On the other hand, a comparison with other student theses avoids violations of my personal copyright.

City and Date	*Signature*

Abstract

Photoelectrochemical water splitting appears to be a promising replacement for fossil fuels as an easily accessible source of energy. Cuprous oxide (Cu_2O) seems to be an ideal p-type absorber semiconductor for a photoelectrochemical (PEC) cell, providing a suitable band gap to perform hydrolysis under visible light. The main challenge with this material is its strong tendency towards photocorrosion, causing instabilities in creating photocurrent.

Through optimization of the applied voltage in electrochemical deposition (ECD) of Cu_2O, this problem is being explored. Also, modifying additional layers, like the choice of material for an optimal p-n-junction or the layer thicknesses deposited via sputtering are being investigated. Furthermore, the cell's testing environment (inert gas purging, electrolyte composition and pH value) is being studied. The testing is carried out under chopped 1.5 AM one sun illumination in an acidic environment with a three-electrode- setup.

By increasing the applied potential for the nucleation process for ECD, a much more compact and uniform absorber layer has been grown. Additional Zn(O,S) as a buffer layer and niobium doped titanium dioxide for passivation fills remaining holes in the absorber layer, provides a p-n-junction for efficient charge separation and protects Cu_2O from corrosion. An electrolyte environment with a pH value of 3 has proven to be most effective in creating photocurrent.

This way, unprotected cells have shown to deliver current densities of up to 2.35 mA/cm^2, which equals a solar-to-hydrogen (STH) efficiency of 2.9%. Cells with additional window layers provided stable photocurrent of 1.1 mA/cm^2 even without using a photocatalyst, which makes this set-up a promising candidate for future PEC cells.

Research is what I'm doing when I don't know what I'm doing.

– Wernher von Braun

Preface

This work is a product of many months in the lab, reading until my eyes were dry, study-sessions with friends and colleagues and of course plenty of coffee. It would not have been possible without the contribution of numerous people, supporting and assisting me academically, as well as mentally. I am very grateful to have had the chance of doing all the experimental research for this thesis at the AIT Austrian Institute of Technology in Vienna. I very much enjoyed the warm and welcoming working atmosphere, as well as the availability of great equipment, machines and especially trust to operate them.

The person having supported me by far the most at my time at AIT, is my dear co-supervisor Dr. Theodoros Dimopoulos. I thank him very much for his time and energy, his patient explanations of complex topics, his input, ideas, and many interesting literature recommendations. Another counterpart, who always made time for me if any issue arose or explanation was necessary, is Dr. Adhi Wibowo. Equally as important was him always being cheerful and passing on good mood for the entire working group.

As for my supervision on the part of the Vienna University of Technology, I would like to thank Ao.Univ.Prof. Dipl.-Chem. Dr.rer.nat. Matthias Weil, who offered guidance and support.

Another big thank you goes out to my all-time best friend Amina. I am beyond grateful for the numerous co-working sessions and her encouraging and cheering words. Same goes for my initially colleague, and now close friend, Kathi. It was a pleasure researching and writing our theses simultaneously and still sharing a never-ending love for matcha latte and blue-orange-bagels with.

Lastly, I owe my parents great appreciation and gratitude for always unconditionally supporting me in every way: My mom especially for providing emotional support, ensuring words and empathy during hours-long phone calls, and my dad for showing interest in the actual details of this research and being one of few people I can and love to have chemistry-related discussions with.

Thank you all so much!

Vienna University of Technology 2021,
Jana Katharina Kupka

Table of content

1. Motivation

The consequences of the climate crisis, such as limited water supply, food supply, extreme weather conditions and change in topography, are global ones and will be affecting the entire humanity sooner or later. One of its causes are greenhouse gases (GHGs), hindering solar radiation from being reflected and therefore resulting in the warming of certain regions.[1]
Consequently, through melting glaciers and ice caps and their water migrating into the ocean, the sea level is rising. This leads to a shrinkage of clean water supplies through pollution and infiltration of freshwater with oceanwater. It is also a reason for negatively influenced crop yields, along with climate extremes, for example extreme temperatures, floods and droughts. Those extremes might also force people to leave their homes due to having become uninhabitable. Another reason, why limited availability of food can be expected, is because weeds, pests and fungi prosper especially well in a warmer environment. [2]

The accessibility of alternative, renewable energy sources has become a global issue mainly due to the current climate crisis. The goal of preventing the planet's temperature increasing 2°C since the start of industrialization cannot be addressed without concentrating on the world's greenhouse gas emissions. [3] Especially carbon dioxide, which makes around 76% of all greenhouse gases, is the most prominent one emitted globally, whereas methane (16%), nitrous oxide (6%) and fluorinated gases (2%) make only about a quarter of all GHGs. Since 65% of all anthropogenous CO_2 is due to fossil fuels and industrial processes [4], carbon-free energy sources are needed. Especially in the transport sector, which draws 95% of its energy from petroleum-based (mainly gasoline and diesel) sources, a renewable alternative is desirable. [4]

Further on, not only the climate crisis, but also the increasing demand in energy due to humanity's changes in lifestyle towards higher energy consumption and general population growth, is motivational in the process of finding alternative fuels. [5]
A great amount of energy nowadays is being used in order to produce electricity. In the 35-year span of 1985 to 2020, the electricity production has risen from around 10000 TWh to more than 25000 TWh, which is 2.5 times as much. Coal-power has steadily been the source for around 40% of electricity production and still is the main contributor. Nevertheless, in the past 7 years, a decrease in the usage of coal was noticeable. Other renewable sources, including wind, water, nuclear and solar energy, altogether make around 36.7% and rising. [6]

A constant supplier of great amounts of energy is the sun, which is one reason, why solar has become the new star in terms of electricity generating technologies. With the help of carefully designed solar cells, it is possible to harvest energy and generate electricity in a sustainable manner. Solar energy being spread across the entire globe is an advantage and a challenge at the same time. Solar energy is available to every country and therefore avoiding emergence of only few suppliers, as in the case of fossil fuels. On the other hand, solar energy being distributed over a large surface area, hence not being concentrated, makes it more difficult for it to be efficiently harvested, since one would need to cover large areas with solar cells. Also, the distribution through the power grid is challenging. Therefore, increased efficiency, along with minimal fabrication cost are of utmost importance for the large deployment of photovoltaics. Furthermore, the challenge is not only to find economical ways to harvest, but also to convert and store the sun's delivered energy effectively and to be able to create a good infrastructure in terms of energy distribution. [7]

As of 2019, solar energy can be transformed into electricity by single-junction solar cells with an efficiency of up to 29.1% (GaAs thin film). Entire modules can perform with a slightly decreased efficiency of up to 25.1% (GaAs thin film). [8] Nonetheless, these Gallium Arsenide cells find their application in a small niche only, due to the high material's cost. Silicon wafer based solar cells are dominating the market (>90%), which provide power conversion efficiencies of up to 26.7% for the cell and 24.4% for module level. [9] Concerning the economic aspects of solar energy, an enormous decrease in production cost for up-scaled PV cells is noticeable. Within the years from 2009 to 2020, the global mean of costs has shrunk from 359 \$/MWh to 37 \$/MWh, which is equivalent to a reduction of almost 90%. One of the reasons is improved technologies, leading to lower capital costs. Also, as the production capacity globally rises, the costs decrease following economics of scale. In 2013, coal's cost leveled with PV (105 \$/MWh), but since then did not change significantly. [10] It is also important to note, that solar cells' costs are highly dependent on the materials and resources used. Furthermore, "hidden" costs, for example those arising due to compensating environmentally unfriendly behavior (e.g. causing GHG emissions or other sorts of pollution) or issues recycling a plant's components after it has reached its lifetime, typically are not included in such statistics. The availability of certain key materials is also a relevant issue affecting the cost.

1.1 Hydrogen as fuel

Most hydrogen on this planet is bound to oxygen in the form of water. Due to the non-toxic, easy to handle and abundant nature of H_2O, it is not only the most convenient, but also the safest and cheapest storage molecule for H_2. [11] The storage and usage of gaseous hydrogen very attractive, because of its wide range of possible applications. Especially in the field of transporting goods and logistics, this type of energy can be beneficial over exemplarily transportation powered by electricity coming from batteries. The latter come with the disadvantage of demanding frequent battery charging and therefore limited distance to cover, which is not an issue with hydrogen. Generally, storing the un-used renewable electricity into hydrogen solves the problem of the sun's seasonal and daily variations, permitting the use of the energy when this is needed. Furthermore, using the sun's energy to convert energy, enables making the switch from grey or blue towards green hydrogen.

Currently, more than 95% of hydrogen produced stems from fossil fuel (grey hydrogen). The remaining 5 % (green hydrogen) are derived using renewable technologies, electrolyzing water into O_2 and H_2. [12] Commercialized technologies for electrochemical water splitting use Proton Exchange Membrane (PEM) or Alkaline Water (AW) electrolyzers connected to the electricity grid or directly to a renewable source, like PV modules. A PV-driven electrolyzer (PVE) consists of two devices: a PV module, responsible for the current generation from solar irradiation and an electrolyzer performing the actual water splitting reaction under usage of the PV-supplied electricity. Alternatively, photoelectrochemical (PEC) cells directly convert sunlight into hydrogen through water electrolysis, within one single device.

Even though PEC systems are not available on the market yet, they provide great potential in making hydrogen production economically competitive, as they could address certain shortcomings of commercialized PVE technologies. For example, AW electrolyzers present slow reaction kinetics under non-optimized operation conditions of power supply. Their sweet spot for working efficiently is limited and minor deviations in supplied power (due to variations in sun irradiation or wind) can reduce the H_2 production. PEM electrolyzers provide faster reaction kinetics and an efficiency of up to 80-90 % of electricity-to-H_2 production. [13] However, PEM electrolyzers need noble and extremely rare metals as catalysts (e.g. Pt, Ru, Ir), which increases their cost and poses a great challenge for up-scaling this technology. Especially since there is no straight-forward alternative for noble metal replacement as PEM-catalysts, as these catalysts need to be stable in highly acidic conditions, where only noble metals excel. [14]

So in conclusion PEC cells, although not commercialized, could be advantageous over PVE technologies in terms of more facile device setup , but also from the point of view of materials costs and H_2 production efficiency. [15]

1.2 (Photo)electrochemical water splitting

The chemical reaction of water splitting (III) consists of two half reactions, which are the oxygen evolution reaction OER (I) and hydrogen evolution reaction HER (II). In total, this non-spontaneous reaction has a positive free Gibbs energy change of $\Delta G = +237{,}2\ kJ/mol$.

$$H_2O \rightarrow \frac{1}{2}O_2 + 2H^+ + 2e^- \qquad (I)$$

$$2H^+ + 2e^- \rightarrow H_2 \qquad (II)$$

$$H_2O \rightarrow \frac{1}{2}O_2 + H_2 \qquad (III)$$

The required energy to perform this reaction, derives from two parameters: The redox potential for H^+/H_2 (HER) and the one for O_2/H_2O (OER). With them amounting 0 V vs. NHE (HER) and 1.23 V vs. NHE (OER), respectively, the overall energy barrier to photolyze water per electron transferred is 1.23 eV, which corresponds to the need of photons of a wavelength of 1000 nm or shorter. [16]

In reality, because of slow reaction kinetics and various energy losses, higher applied potential, the so-called overpotential, is needed to achieve considerable reaction rates and net current flow. This is why the actual operation potential for water electrolysis lies somewhere from 1.6 to 2.2 V eV. [17] [11] This means that the band-gap of the absorber material in the PEC photocathode or photoanode needs to be in this range in order to initiate the desired reaction. [18].

For the HER, an on the electrode (photocathode) adsorbed hydronium cation's (H_3O^+) proton reacts with an electron. Joined with another adsorbed hydrogen atom, gaseous hydrogen evolves und desorbs from the electrode. The bottleneck of the slow reaction kinetics in PEC water splitting is the OER, for which larger overpotential is needed compared to HER. To increase the reaction rates, catalysts are implemented to facilitate the HER and OER. Most active, commonly used ones would be metal oxides, such as RuO_2, NiO, CoO, but also perovskites and tertiary oxyhydroxides for the OER and Pt for the HER. [19]

Depending on the materials used or the cell's reaction environment, side reactions are also possible (IV). One the one hand, back reactions from water splitting products can occur.

In particular, the reaction of hydrogen and oxygen through oxygen reduction reaction (ORR). [20]

$$H_2 + \frac{1}{2}O_2 \rightarrow H_2O \qquad \text{(IV)}$$

Other ORRs, especially favored by some noble metals, for example Au, are those in O_2 or H_2O_2, which are both side products of the photoelectrochemical water oxidation. Hereby, the reacting hydrogen does not stem from already formed hydrogen gas, but rather from excess hydron found in highly acidic electrolytes (V). [21]

$$\begin{gathered} H_2O_2 + 2H^+ + 2e^- \rightarrow\ 2H_2O \qquad \text{(V)} \\ O_2 + 4H^+ + 4e^- \rightarrow 2H_2O \end{gathered}$$

Another reaction, is the self-reaction of hydrons from acidic solutions forming H_2 (VI). [21]

$$2H^+ + 2e^- \rightarrow\ H_2 \qquad \text{(VI)}$$

1.3 Photoelectrochemical cells

A PEC cell can be custom designed, depending on material availability. Nevertheless, there is a general structure which is being followed in terms of combining certain material groups with specific functions (Figure 1). A conductive substrate always sets the base for building a PEC cell. Followed by a photosensitive semiconductor absorber layer, which generally makes the thickest functional layer, within the µm range, as it needs to absorb the light as thoroughly as possible. The window layer, consisting of buffer and passivation layer, is usually in the 20-100 nm range. A co-catalyst is optional and typically makes only very few nm in thickness and in most cases has the form of islands.

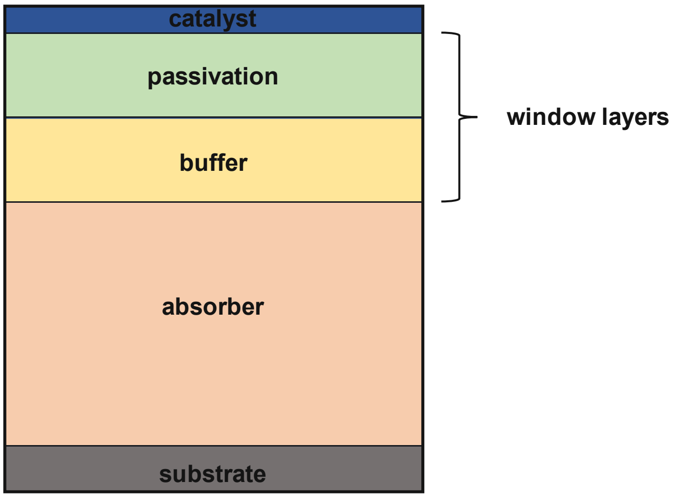

Figure 1: General architecture of a PEC cell

1.3.1 Absorber layer

The centerpiece of a PEC cell is the semiconductor absorber layer, since it determines the possible amount of solar energy being harvested. Natural sunlight reaching the earth's surface consists of UV (6.6%), visible (44.7%) and IR (48.7 %) radiation. [22] Altogether, the sun delivers energy with wavelengths in the range of around 300 to 2500 nm. Even though there is no material able to be sensitive in the entire solar spectrum, the aim is to find ones, which cover a great portion of it. [23] Furthermore, there is the criteria of providing the earlier mentioned minimum band gap of ~1.6 eV (~800 nm) to drive the electrolysis reactions. [24] With choosing a semiconductor regarding its band gap, there has to be a compromise made. For once, utilizing low band gap semiconductors is ideal in order to absorb the majority of photons, provided by sun light. On the contrary though, larger band gap materials are preferred to provide enough energy to overcome the overpotential for the actual water splitting reaction. [25] An additional factor is the charge carrier's diffusion length in the semiconductor. A semiconductor's thickness should not be greater than said diffusion length, since charge carriers would more probably recombine before reaching the respective electrodes. [26]

For the purpose of a photocathode, the absorber is a p-type semiconductor, for which the conduction band lies higher than the energy level of the HER (see Figure 2). Photo-generated electrons can thus be transferred from the CB of the semiconductor to the HER level. The hole from the VB of the photocathode is transferred to the anode through the electrical circuit, where it is consumed to for the OER. For this to happen without externally applied potential, the OER level should be above the semiconductor valence band. Therefore, specifically, the p-type semiconductor's conductive band minimum must be greater than 0 V vs. NHE, whilst the valence band maximum has to lie below 1.23 V vs. NHE. Suitable margins should be added to account for the needed overpotentials. Most p-type photocathodes (including Cu2O) have favorable energetics only for HER but not for OER. n-type photoanodes are used as photoanodes, as their energy band positions favor the OER reaction. [27]

With the requirement for above mentioned band gap energies, the issue of self-oxidation and self-reduction upon illumination arises. These effects often occur in semiconductors with their redox potential lying within the water splitting reaction's potential window and are the main reason for a PEC cell's decreased stability (Figure 2). Photocorrosion is a problem with materials exposed to aqueous solutions, which is a great disadvantage of PCE against PVE systems. [27]

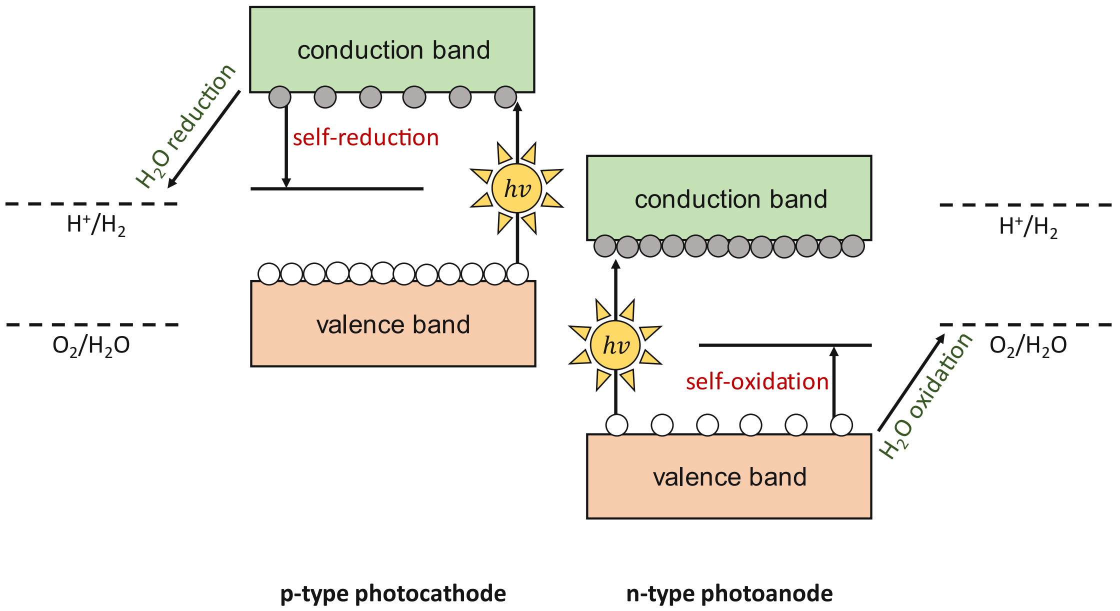

Figure 2: Photocorrosion in photoelectrodes

Depending on the position of the semiconductor's redox potential relative to the water splitting redox potential, either self-reduction, self-oxidation or both reactions are possible. In the case of reduction, photogenerated electrons in the conduction band reduce and therefore decompose the semiconductor material. Analogous, if valence band holes react with the photoelectrode instead of oxidizing water, it results in self-oxidation, as displayed in equation VII. [27]

$$MX + ze^- \rightleftharpoons M + X^{z-}\ (reduction) \tag{VII}$$
$$MX + zh^+ \rightleftharpoons M^{z+} + X\ (oxidation)$$

Since most semiconductor materials suitable for electrochemical water splitting are prone to light-induced self-corrosion, this problem is almost unavoidable. Currently, the focus is on working with the given materials and trying to prevent self-corrosion as good as possible, using for example passivation (protective) layers against corrosion. Figure 3 gives an overview of common photo absorbers for water splitting. The green columns illustrate the valence bands' positions, whereas the blue ones represent the conduction band minimum. The dashed lines within or in between show the material's oxidation (red) and reduction (black) potentials relative to NHE, while the dashed black and red lines are the HER and OER levels, respectively. Materials stable against photocorrosion need to have their redox potentials outside the bandgap. Exemplarily, ZnO's reduction potential is above the CB minimum, so it is stable against self-reduction. Nonetheless, ZnO’s CB minimum lies below 0 eV vs. NHE, making it not ideal for performing HER. As for Cu_2O, the CB and VB positions are suitable for HER and OER, since they lie outside water’s redox potential regime. However, with cuprous oxide’s redox potentials both being within the bandgap, it is a material prone to self-oxidation, as well as -reduction. So, a suitable semiconductor would have its conduction band minimum, as well as reduction potential above HER and its valence band maximum, as well as oxidation potential below OER.

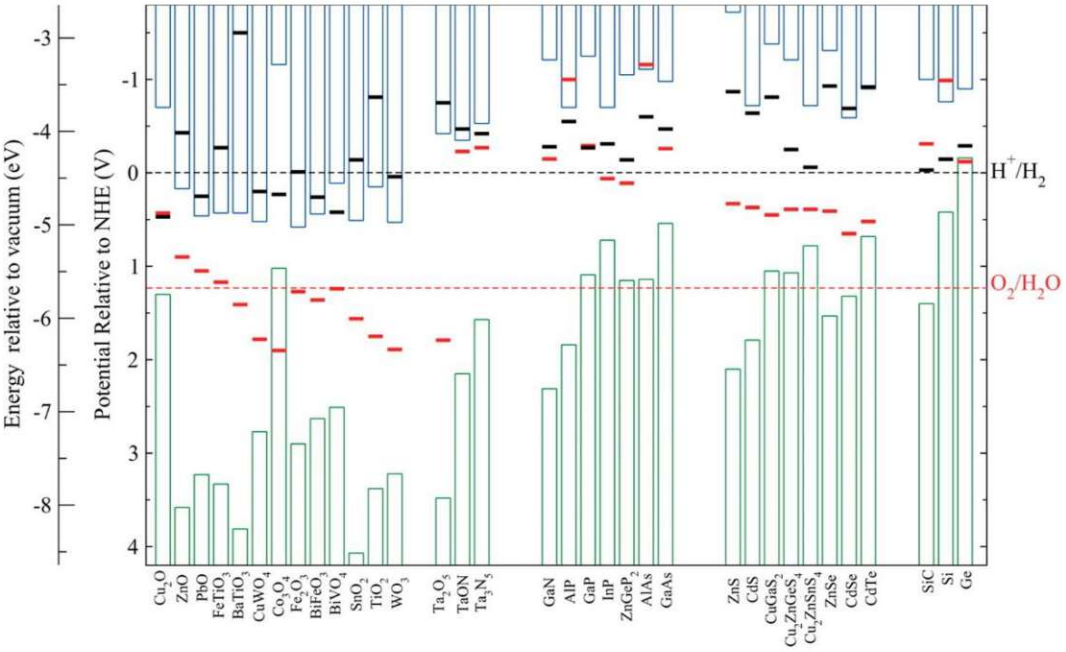

Figure 3: Various semiconductors' band gaps and redox potentials [28]

1.3.2 Window layers

Through the absorption of a photon containing sufficient energy, an electron from the semiconductor’s valence band is excited to the conductive band, leaving a hole h^+ in the VB and creating a free electron e^- in the CB. In order to prevent those charge carriers from recombining and to promote charge transfer to perform further reactions, a junction comes into play. This junction can be formed between the absorber and the electrolyte, in which case it is a Schottky junction. Alternatively, a solidstate p-n junction can be formed, by depositing an n-type semiconductor (that we call buffer layer) on top of the p-type absorber.

So, the n-type buffer layer, which is part of the window layers, combined with the p-type absorber, creates the p-n junction. Its role is to foster the separation of electron-hole pairs, through the created built-in electric field, and therefore boost the overall water splitting performance. [29] The buffer has also to be as transparent as possible (to allow the light to pass into the absorber), so high bandgap semiconductors are used.

In a p-type semiconductor, holes are majority carriers, whereas in an n-type one [30], it is the electrons. If the two semiconductors are brought in contact, the large charge density gradient causes diffusion of mobile electrons towards the holes (from the n to p region) and vice versa. At the proximity of the p-n interface, a so-called “depletion area” is formed, depleted of free carriers and composed of immobile donor and acceptor ions (Figure 4). [31] The electric field thus arising at the p-n-junction stops the further flow of free charge carriers over the junction and an equilibrium state is attained. (Figure 4).

When photons create photogenerated electron-hole pairs in the p-type absorber, the pairs are separated by the internal electric field, with the electrons moving towards the n-type material and then to the photocathode/electrolyte interface for the HER to take place. [32] At the PEC-system’s counter electrode (anode), electrons from the electrolyte solution are pulled towards the anode, resulting in oxidation reactions on the surface (OER). Electrons then flow through an external circuit towards the photocathode, creating photocurrent, where they will recombine with holes from the p-type material (Figure 5). [26]

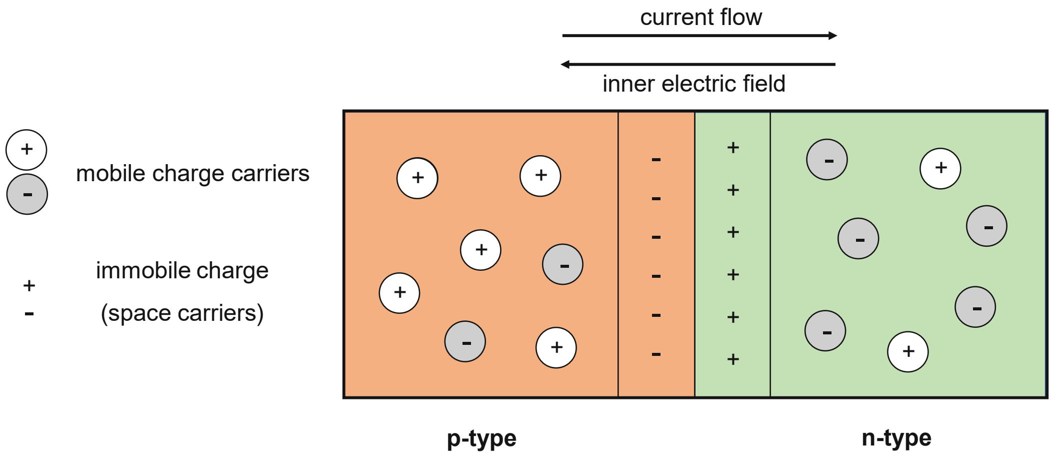

Figure 4: Solid/solid junction in a PEC cell and the distribution of mobile and immobile charge carriers (electrons and holes) in the p-type and n-type semiconductor

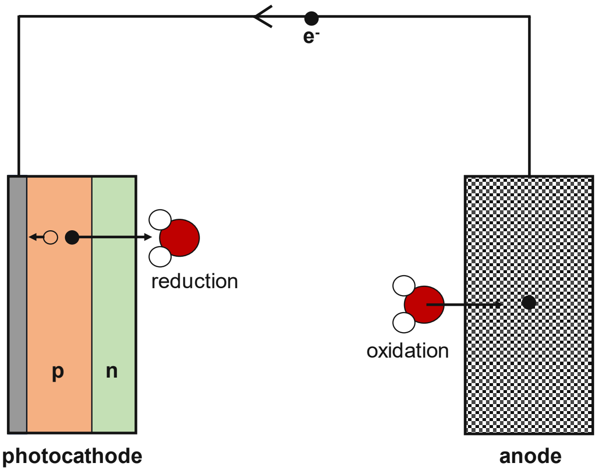

Figure 5: Reaction scheme of photogenerated minority charge carriers in a PEC cell under the usage of a photocathode

Since the n-type semiconductor buffer layer being directly exposed to an eventually highly acidic electrolyte can cause fast degradation, an additional n-type passivation layer can be beneficial. It functions as a protective layer.

In such heterojunctions, when p-type and n-type materials are being combined, their energy band alignment is crucial. Depending on the materials' conduction band minimum $E_{CB,min}$ and valence band maximum $E_{VB,max}$ positions relative to each other, there are three different alignment possibilities (Figure 6).

For the straddling type I, one semiconductor's band gap fully contains the second one's. In this case, electrons from the p-type absorber's conduction band CB1 cannot be transferred to the n-type semiconductor buffer's CB2, neither can holes from VB1 to VB2.

The staggered gap type II is the preferred one, since it promotes charge carrier transfer and separation. [33] Since the two band gaps overlap, the process of charge carriers moving is no longer symmetrical. For example, in a p-type absorber semiconductor, electrons from CB1 can be transferred towards the n-type buffer's CB2. Simultaneously, holes from VB1 cannot be transferred to VB2, due toa potential barrier for holes being present). This makes type II gaps favored since each carrier type can only be transferred towards one direction. As a consequence, their recombination is hindered and transport towards opposite electrodes is enabled. Type II is the band gap alignment occurring in a Cu_2O/ZnO or Cu_2O/ZnOS junction.

The third type is the broken gap type III. In this case, there is no overlapping at all. In terms of charge carrier behavior, it is rather similar to type II, since electrons can only be transferred from CB1 to CB2, whereas holes bounce back on their way from VB1 to VB2. [34] [35] Additionally, charge carriers can also be exchanged between VB1 and CB2, due to them being closely placed towards each other. This fact might cause issues, which is why type II is preferred over type III.

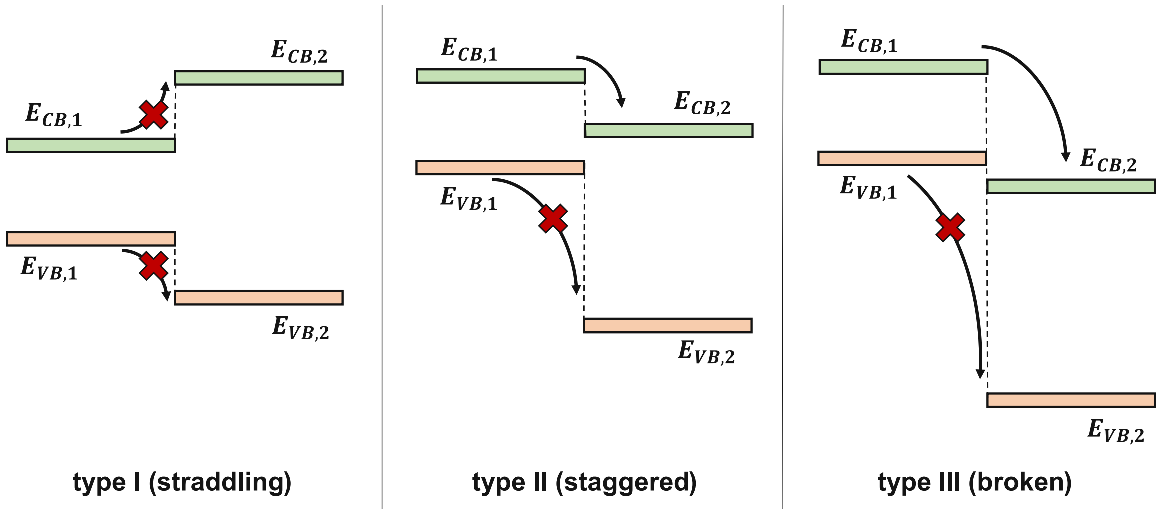

Figure 6: Different types of band gap alignments with the positioning of the absorber's (1) and buffer's (2) conduction and valence band energy levels. The arrows describe whether or not electron transfer between conduction bands or hole transfer between valence bands is possible.

It is also important to note, that defects, which can easily occur during interface formation, can again contribute to the altering of the band structure of the material and therefore the band alignment. Exemplarily for Cu_2O as a p-type material, the possibility of self-redox reactions occurring and therefore Cu or CuO forming is relatively high. Subsequently, those species can then as well cause modification of energy band alignment. [36]

Overall it can be said, that the energy band alignment at the heterojunction largely influences the PEC performance, as it determines the charge carrier separation and transport towards the electrolyte and back electrode for the participation in the HER and OER, respectively. [33]

1.3.3 Co-catalyst

Photoelectrodes are very often being modified with co-catalysts. An ideal co-catalyst provides active sites for HER and OER. To design a cell with optimized solar-to-hydrogen (STH) efficiency, two types of co-catalyst would be needed. A HER co-catalyst accelerates the process of promoting proton to hydrogen reduction. Respectively an OER co-catalyst would boost the water oxidation reaction. Enhancing the two half reactions increases the overall activity of a water splitting system. These processes are realized through the co-catalyst lowering the reaction's activation energy and therefore decreasing the energy barrier (Figure

7). [37] Most commonly, reduction co-catalyst are made from noble metals, such as Pt, Pd, Rh or Au, whilst materials promoting the oxidation reaction usually are metal oxides, such as RuO_2 or IrO_2. [37]

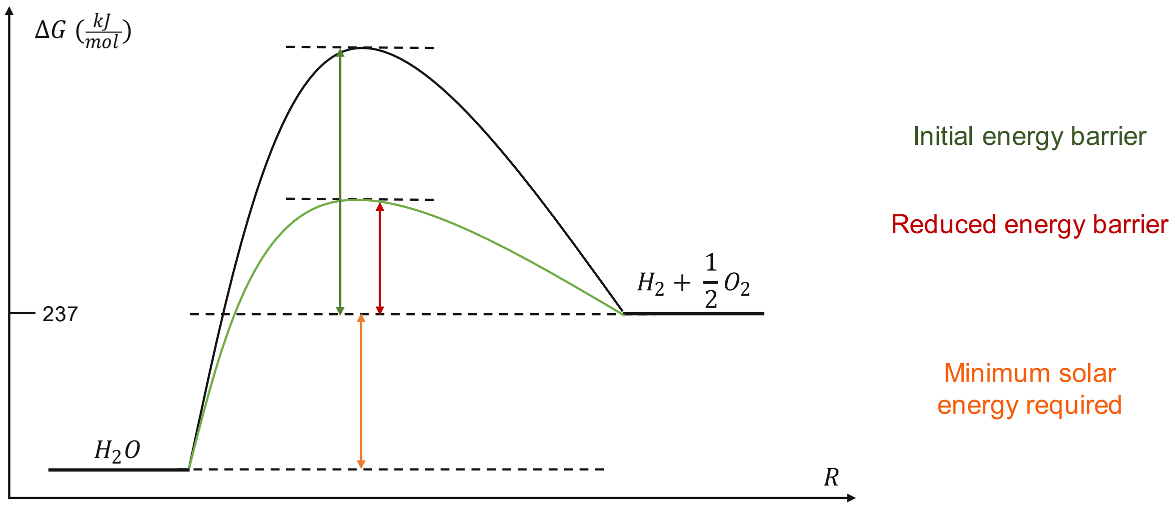

Figure 7: Working principle of a co-catalyst for water splitting

The half reaction with slower kinetics is determining the overall reaction's rate. In water splitting, this is typically the case for the oxidation reaction requiring a greater overpotential than HER. [37]

1.3.4 Evaluating a PEC cell

A critical figure for the evaluation of a PEC cell performance is the solar-to-hydrogen (STH) efficiency.

$$STH = \frac{output\ energy\ in\ the\ form\ of\ H_{2\,(g)}}{energy\ of\ incident\ solar\ light} = \frac{r_{H_2} * \Delta G}{P_{sun} * A} * 100\% \qquad (VIII)$$

In equation (VIII), r_{H_2} stands for the rate at which hydrogen is being produced (mmol/s), ΔG is the gain in Gibbs free energy per mole of H_2 (=237 000 J/mol at 25°C), P_{sun} is the sun's energy flux (mW/cm²) and A describes the illuminated area (cm²). With the thermodynamic reversible potential for water-splitting ($\frac{\Delta G}{nF}$), this equation can be simplified, as displayed in equation IX.

Here j_{ph} is the system's photocurrent density and P_{in} is the power density of the illumination (100 mW/cm^2 for the AM 1.5 spectrum that is used in the present experiments). [38] Often the assumption of the faradaic efficiency η_F being 100 % is made. This would imply, that charge used for HER and OER is equal to charge flow through the cell's external circuit. This way, the efficiency can be calculated without even measuring the amount of hydrogen generated. In reality though, η_F can be less that 100%, if side reactions occur. [39]

$$STH = \frac{j_{ph} * \ 1.23\,V * \eta_F}{P_{in}} \qquad \textit{(IX)}$$

So generally, STH efficiency is the ratio of chemical energy in gaseous H_2 with respect to the illumination energy input the cell is exposed to.

Another way of evaluating a photoelectrochemical cell is by its incident-photon-to-current conversion efficiency (IPCE), resolved for different wavelengths. It is defined by the number of electrons generated per incident photons, for each wavelength. The IPCE (equation X) is given as a function of the light's wavelength λ, since it incorporates the current density j_{ph} measured under monochromatic illumination. Here, e is the electron's charge, h the Planck's constant, c the speed of light, which altogether result in a constant of 1239.8 V*nm. [39] Even more significant is the absorbed-photon-to-current conversion efficiency (APCE), which takes into account the number of generated electron/hole pairs (e^-/h^+) (equation XI), subtracting light losses due to reflections etc.

$$IPCE(\lambda) = \frac{electrons\ (cm^{-2}s^{-1})}{incident\ photons\ (cm^{-2}s^{-1})} = \frac{\frac{j_{ph}(\lambda)}{e}}{P_{mono}(\lambda) * \left(\frac{hc}{\lambda}\right)} \qquad \textit{(X)}$$

$$APCE(\lambda) = \frac{IPCE(\lambda)}{\eta_{e^-/h^+}} \qquad \textit{(XI)}$$

Typically, current densities and power intensities are measured in increments of 5-20 nm. For deriving the current density, fixed potential is applied, and values are recorded as soon as steady state is reached. IPCE is a product of the three main processes' efficiencies η relevant in water electrolysis: charge generation, -transport and -transfer, as shown in equation XII.

$$IPCE(\lambda) = \eta_{e^-/h^+} * \eta_{transport} * \eta_{transfer} \tag{XII}$$

In order to calculate a PEC cell's non wavelength specific, total current density, individual photon-to-current conversion efficiencies are integrated over the AM 1.5 solar spectrum. In equation XIII, E(λ) is the used light source's energy. It is a way of validating current densities derived from experimental measurements, since the calculated values should match. Some exceptions are possible with certain materials. [39]

$$j_{ph} = \int IPCE(\lambda) * \frac{E(\lambda)}{\frac{hc}{\lambda}} * e d\lambda \tag{XIII}$$

1.3.5 The Challenge

When designing a PEC cell, several boundary conditions need to be taken into consideration, concerning:

- Material properties
- Cost of materials and fabrication processes
- Ecological impact

Especially regarding the materials used, there are multiple parameters having a great impact on the overall systems performance. Not only the materials' individual properties are crucial, but their combination determines the overall device's functioning. Exemplarily, by varying materials or deposition processes, the band structure alignment can change as well. This, in further consequence, impacts the process of charge carrier transport. Ideally, the sample's constituents complement each other to optimize the PEC cell in terms of light absorption, charge separation, charge transport and catalytic activity for the HER and OER. Another factor strongly connected to these fundamental required properties, is the cell's working environment. Decreased stability and degradation due to strongly acidic or basic electrolytes in combination with illumination have been a common problem with photoelectrochemical systems.

Economic matters are also of utmost significance since they define whether or not future upscaling and commercial viability is realistic and reasonable. As for the ecological impact, it is important that non-toxic materials and processes are deployed in the future at industrial scale.

Especially with new technologies, there is a great focus on green(er) alternatives, which is vital for humanity to proceed living on this planet and prevent it from being even more harmed. Those three parameters are strongly intertwined and influence each other, which is why they all need to be taken into account with equal significance.

2. Approach followed in the thesis

2.1 Materials

The main aim for this study, was to investigate Cu_2O-based PEC photocathodes, which material components consist of abundant and low-environmental materials and are fabricated using up-scalable, state-of-the-art techniques, like electrochemical deposition and sputtering. The largest challenge is to create a device providing good efficiency, along with high stability over a long period of time. For this to be realized, it is inevitable to pay attention to a PEC photocathode's each individual layer, but also to the device as a whole, with special focus on the materials forming the p-n junction.

The first material we need to look at is the substrate upon which the photocathode is built. Most common substrate for PEC electrodes is the plain glass substrate coated with a thin layer of a transparent conductive oxide (TCO), specifically tin-doped indium oxide (ITO) or fluorine-doped tin oxide (FTO). Other layers can be added, to enhance the TCO adherence, influence the crystal structure, or modify its energetics (e.g. use an interfacial layer to selectively collect the holes).

The substrate of choice for the upcoming experiments was glass/ITO. As a rather unusual alternative substrate material, photocathodes build on steel were investigated as well. In this case, a low-cost, stainless-steel foil was used as substrate. An additional benefit of having foil as a base, is the possibility of eventually depositing the photocathodes by roll-to-roll processing, since foil provides flexibility during production. Stainless steel is also a low cost substrate, compared to the TCO-coated glass.

Apart from the PEC device centerpiece, the p-Cu_2O absorber layer, a buffer layer is needed. It forms the p-n junction with the absorber, enhancing the electric field, preventing self-reduction and increasing the PEC cell efficiency, as well as stability. [40] Compounds, which have proven to be suitable candidates as n-type layers in combination with Cu_2O, are n-ZnO and n-ZnOS.

Further, the passivation layer functions as a protective overlayer enhancing the overall stability. They prevent the absorber material from degradation through eventual chemical side reactions by separating the semiconductor material from the rather hash conditions of the electrolyte environment common for PEC applications. [41] The focus in this thesis was on titanium oxide overlayers, especially niobium-doped TiO_2 (NTO). These layers are stable against photocorrosion in aqueous solutions, and they do not impede the electron transport from the absorber towards the electrolyte for the HER to take place.

Typically, noble metals (especially Pt) or transition metal oxides (NiO, Co_3O_4) are being used as co-catalysts for PEC photocathodes. They were shown to reduce the reaction barrier height for the HER. Since platinum is an expensive, non-abundant material, cells with no catalyst at all were synthesized, as well, and compared to those with a thin layer of Pt.

2.2 Techniques

An additional way to pursue the goal of being economic and ecological at the same time, is to minimize the overall deposition process' complexity. Especially with commercialization in mind, it is inevitable to make the up-scaling process as facile as possible. Alongside keeping said process simple and quick to perform, the issue of achieving the same or even similar efficiencies on a greater scale arises. Generally, the larger a PEC's area, the worse its performance, due to a higher probability of generating defects along the production process.

Within this work, two main processing methods were chosen for the entire fabrication of the complete PEC cell. The growing of the absorber layer (p-Cu_2O) was solely done by electrochemical deposition (ECD), whilst the remaining layers were deposited using sputtering. Both techniques are widely-used industrial techniques and compatible with both batch-to-batch and roll-to-roll industrial processing. In many reports, atomic layer deposition (ALD) is applied for the deposition of thin buffer and passivation layers, as this technique has an unparalleled advantage in homogeneously covering 3D, rough surfaces. Sputtering, as a directional deposition technique, does not share this characteristic and therefore the coverage of rough surfaces is not optimal. On the other hand, sputtering has a competitive advantage in fast processing against ALD.

All photocathodes were illuminated using a Xenon lamp providing AM 1.5G spectrum illumination (100 mW/cm^2), calibrated with a Si solar cell. The so-called air mass (XIV) is defined by the angle, at which solar light travels through the atmosphere towards the earth's surface. Outside the atmosphere, the spectrum is defined as AM 0. Of course, the effect of solar irradiation on the earth's atmosphere is dependent on location, date, and time. Still, AM1.5G is considered global radiation standard. This value corresponds to an angle of 48° or α=0.841 radians.

$$AM = \frac{1}{\cos\alpha}$$

XIV: Equation for calculating air mass AM under usage of the angle (radians) between the sun and the earth's surface

In reality though, actual solar irradiation is dependent on local conditions and is very often reduced by cloudiness, pollution, humidity or other varying parameters. Looking at the solar energy spectrum under AM1.5G conditions, only the portion above ~1.6 eV provides photons with suitable wavelengths (< 775-689 nm) for PEC water splitting. In reality, losses in energy are expected to move this lower threshold closer to 2 eV, which again limits the actual solar conversion efficiency. [42]

2.2 Architectures

When the photocathode with the bare p-type absorber is immersed into the electrolyte, a Schottky junction is formed between the absorber and the electrolyte that is responsible for the induced electric field. A p-type/electrolyte junction can be identified by the Fermi energy in equilibrium lying closer to the semiconductor's valence band. Holes diffusing towards the electrolyte or electrons migrating towards the p-type causes a negative space charge region to form. This hinders holes from further diffusing and results in a downwards directed band bending (Figure 8).

On the other hand, if a solid-state p-n junction is formed, the semiconductors' individual Fermi energy levels align and consequently an electric field arises in the direction from n- towards p-type semiconductor. Also, some band bending in the contact region of the semiconductor/electrolyte interface occurs, going up (n-type) or down (p-type).

Figure 8 compares the two types of junctions showcasing their components' energy levels at equilibrium in relation to each other.

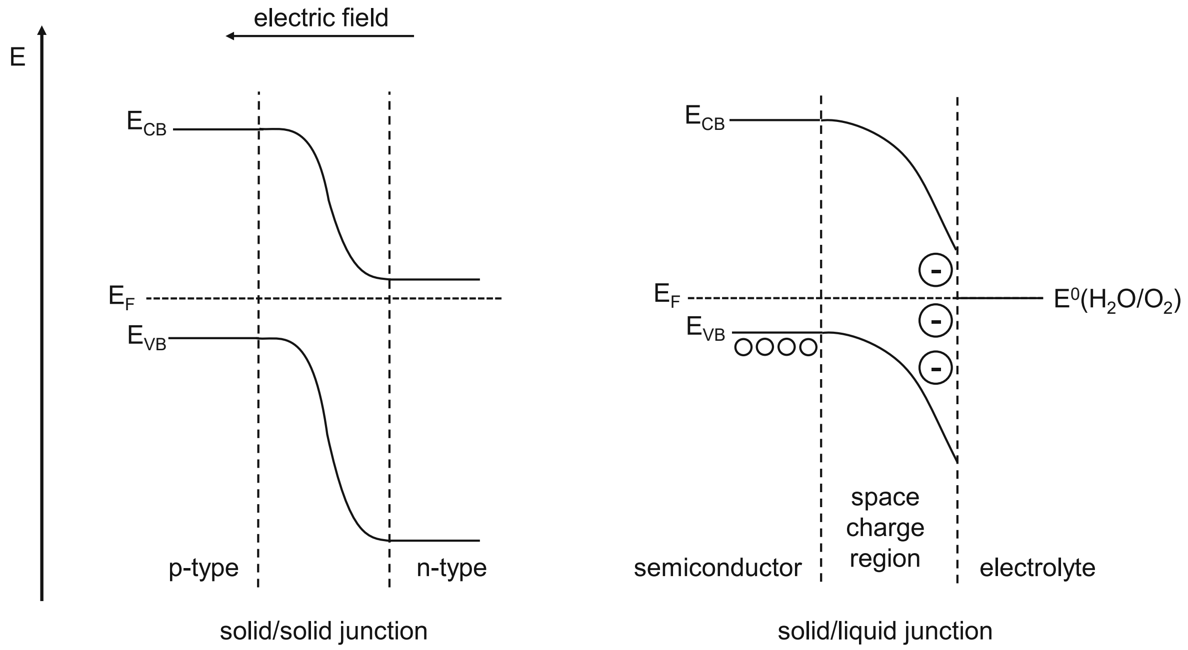

Figure 8: Solid/solid p-n junction at equilibrium (left) with E_F being the Fermi energy level, E_{CB} the conduction band's energy and E_{VB} the valence band's energy. [43] Solid/liquid p-type semiconductor/electrolyte junction at equilibrium (right) with $E^0(H_2O/O_2)$ being the aqueous solution's energy level. [44]

For applications in photoelectrochemical water splitting, a contact with a redox electrolyte is required. This creates another junction between the n-type semiconductor and the liquid: the solid/liquid junction. [45] Moreover, this is the interface, where the desired HER takes place, but concurrently the area most and first impacted by (photo)corrosion. To protect this area from decomposition, additional layer made from very stable n-type NTO and, in certain cases, Pt co-catalyst have been deposited (Figure 9).

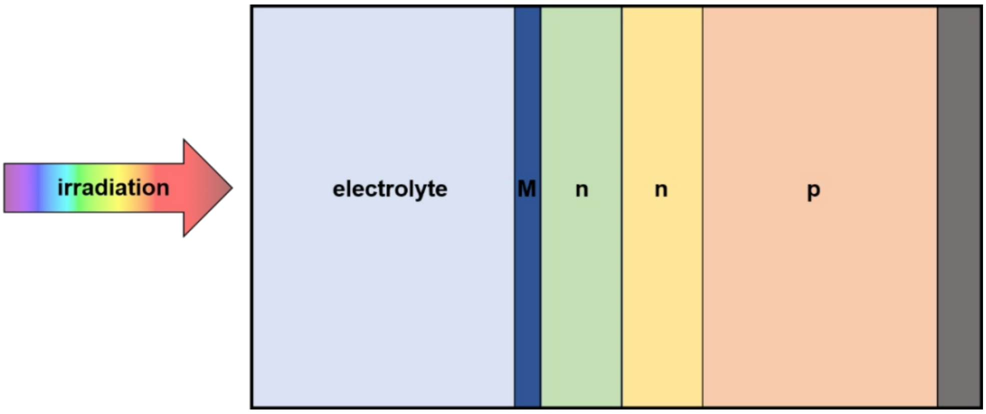

Figure 9: Scheme of a PEC cell in its environment

2.3 State-of-the-art

Table 1 showcases a collection of different PEC cells' performances based on Cu_2O absorber material. They vary in substrate and window layer material, as well as architecture, deposition techniques and testing environments. The rows shaded in grey portray so-called "bare" cells, with no additional window or co-catalyst layers, which explains rather low achieved current densities. The range of generated current is rather broad and can vary from <1 to >10 mA/cm^2. Unfortunately, most researchers did not report about the actually illuminated sample area, which is a critical factor in evaluating current densities. A trend noticeable when comparing these studies, is, that electrochemical deposition is a common choice of fabrication method. Furthermore, applied bias of 0 V vs. RHE appears to be the most efficient testing potential. Contrary to this thesis, literature rarely reports an acidic working environment for the Cu_2O-based PEC cells.

Table 1: Collection of cuprous oxide-based PEC cells from literature alongside experimental details

Substrate (_nm)	**Cu_2O (µm)**	**Buffer (_nm)**	**Co-catalyst (_nm)**	**Cu_2O deposition method**	**Buffer deposition method**	**Co-catalyst deposition method**	**Current density (mA* cm^{-2})**	**Potential applied (V vs. RHE)**	**Electrolyte**	**pH**	**Comment**	**Reference**
FTO/Au_50	1	/	/	ECD	/	/	-0.07	0	0.5 M Na_2SO_4	6.5	illumination area: 0.28 cm^2	[46]
ITO	0.183	/	/	Spray-pyrolysis	/	/	-0.1	0.21	0.1 M NaOH	13		[47]
FTO		/	/	ECD	/	/	-0.6	0	1 M Na_2SO_4	7		[48]
FTO/Cr_20/ Au_200	1.3	/	/	ECD	/	/	-2.4	-0.25	1 M Na_2SO_4 buffered with 0.1 M KPO_3	4.9	continuous N_2 purging	[32]
FTO/Au_50	1	/	NiFe-LDH	ECD	/	ECD	-0.49	0	0.5 M Na_2SO_4	6.5	illumination area: 0.28 cm^2	[46]
ITO	0.183	$SrTiO_3$_160	/	Spray-pyrolysis	Sol-gel spin coating	/	-2.52	0.21	0.1 M NaOH	13		[47]
FTO	1-4.7	CuO/WO_3	/	ECD	Spin coating	/	-1.9	0	1 M Na_2SO_4	7		[48]
ITO/Cr/Au_10		Ga_2O_3_10/ AZO_8/TiO_2_10	Pt_60	ECD	PLD	sputtering	-4	0	0.5 M Na_2SO_4/0.09 M KH_2PO_4/0.01 M K_2HPO_4 buffered with 2M NaOH	6		[49]
Cu foil	1	n-Cu_2O_500/ AZO_30/ TiO_2_30	Pt	ECD	ECD/ALD	PEC deposition	-4.3	0	0.5 M Na2SO4/0.1 M KH_2PO_4	4.15	N_2 purging before measuring; continuous stirring	[50]
Cu foil		NiO_x_10	/	ECD	Spin coating	/	-4.98	-0.33	0.1 M Na_2SO_4	6	nanowire Cu_2O, white-light irradiation (26 mW cm^{-2})	[51]
FTO/Cr_20/ Au_200	1.3	ZnO_21/ TiO_2_11	Pt	ECD	ALD	ECD	-7.8	0	1 M Na_2SO_4 buffered with 0.1 M KPO_3	4.9	continuous N_2 purging	[32]
FTO/Cu_1.5		Ga_2O_3_20/TiO_2	RuO_x	ECD	ALD	PEC deposition	-10	0	0.5 M Na_2SO_4/0.1 M PO_4^{3-}	5	nanowire Cu_2O	[52]

All samples illuminated under following conditions: 100mW/cm^2; AM1.5 illumination

1. Huan Qi, J.W., Denis Fichou, Zhong Chen, *Cu2O Photocathode for Low Bias Photoelectrochemical Water Splitting Enabled by NiFe-Layered Double Hydroxide Co-Catalyst.* Nature Scientific Reports, 2016. **6**(30882).
2. Dipika Sharma, S.U., Vibha R. Satsangi, Rohit Shrivastav, Umesh V. Waghmare, Sahab Dass, *Improved Photoelectrochemical Water Splitting Performance of Cu2O/SrTiO3 Heterojunction Photoelectrode.* Journal of Physical Chemistry C, 2014. **118**(44): p. 25320-25329.
3. Soolmaz Jamali, A.M., *Improving photo-stability and charge transport properties of Cu2O/CuO for photo-electrochemical water splitting using alternate layers of WO3or CuWO4 produced by the same route.* Applied Surface Science, 2017. **419**: p. 269-276.
4. Paracchino, A., et al., *Highly active oxide photocathode for photoelectrochemical water reduction.* Nat Mater, 2011. **10**(6): p. 456-61.
5. Wang, Y.C., et al., *Cu2O photocathodes for unassisted solar water-splitting devices enabled by noble-metal cocatalysts simultaneously as hydrogen evolution catalysts and protection layers.* Nanotechnology, 2019. **30**(49): p. 495407.
6. Tuo Wang, Y.W., Xiaoxia Chang, Chengcheng Li, Ang Li, Shanshan Liu, Jijie Zhang, Jinlong Gong, *Homogeneous Cu2O p-n junction photocathodes for solar water splitting.* Applied Catalysis B: Environmental, 2018. **226**: p. 31-37.
7. Chia-Yu Lin, Y.-H.L., Dirk Mersch, Erwin Reisner, *Cu2O|NiOx nanocomposite as an inexpensive photocathode in photoelectrochemical water splitting.* Chemical Science, 2012. **3**(12): p. 3482-3487.
8. Pan, L., et al., *Boosting the performance of Cu2O photocathodes for unassisted solar water splitting devices.* Nature Catalysis, 2018. **1**(6): p. 412-420.

3. Properties of utilized materials

3.1 Substate

The substrate is the base for the entire solar cell. It has to be electrically conductive enough to perform electrochemical deposition and provide good adhesion and therefore stability for the later deposited absorber layer. It also must be considered that the substrate's surface crystal orientation also might determine the following electrodeposited layer's orientation.

3.1.1 Indium tin oxide (ITO) coated glass

Depositing on indium tin oxide (ITO) (SnO_2-doped In_2O_3) coated glass slides (*Sigma Aldrich*) has the advantage of providing stability for the following layers. With an ITO coating of 120-160 nm, the sheet resistance amounts to 8-12 Ω/sq., making it suitable for electrochemical deposition purposes and as electrical contact for the photocathode. The average visible transmittance of the glass-coated ITO substrate is >85%, which permits illumination of the photocathode also through the substrate. ITO has a bandgap of ~3.6 eV and its work function is ~4.4 eV. [53] ITO is a higher-cost transparent conducting oxide (TCO) but its cost is still dramatically lower than the commonly used Au for Cu_2O PEC cells. Also, a common alternative for Cu_2O PEC cells is FTO (Fluorine doped SnO_2)-coated glass. Although FTO has a lower-cost to ITO, its significantly higher roughness can be a serious disadvantage for the homogeneity of the Cu_2O absorber.

3.1.2 Steel foil

Stainless steel as a substrate is a more sustainable alternative to ITO. In terms of environmental aspects, the possibilities to reuse and recycle are significant. From an economic standpoint, steel has the advantage of being a long-living and well-studied material. Industries are providing great expertise concerning the production process, which lowers overall costs, whilst enhancing the material's quality and reliability. Regarding sustainability, stainless steel is abundant and non-toxic, neither in production, nor in its usage. [54]

As for properties, the used stainless-steel foil has a sheet resistance of 7 mΩ/sq and a thickness of 100 µm. [55] With steel's resistance being lower than ITO's, less bias is needed for electrodeposition at high rates. [56] It has been reported that both [100] and [111] orientated Cu_2O can be electrochemically deposited on polycrystalline stainless steel substrates at alkaline pH. [57] Moreover, steel foil is a flexible material, leaving the option of producing flexible devices, which could be a major advantage when considering up-scalable processes such as roll-to-roll production.

3.2 Absorber layer

Copper compounds come with different properties and characteristics and can be distinguished through their colors. Elemental copper shows the commonly known pinkish-red color, whereas copper(I)oxide appears to be orange-red. Copper(II)oxide is generally a black solid.

Cu_2O belongs to the Pn3 space-group (Pn3m (224)). The cubic Bravais lattice shows oxygen tetragonally coordinating four copper atoms, which are then linearly bound to two more oxygen atoms, as shown in Figure 10. Cu_2O is highly insoluble and thermally stable. It is, besides CuO, which has a hexagonal unit cell, and Cu_4O_3, which has a tetragonal unit cell, one of three stable oxides of copper. Their mineral names are cuprite for Cu_2O, tenorite for CuO and paramelaconite for Cu_4O_3.

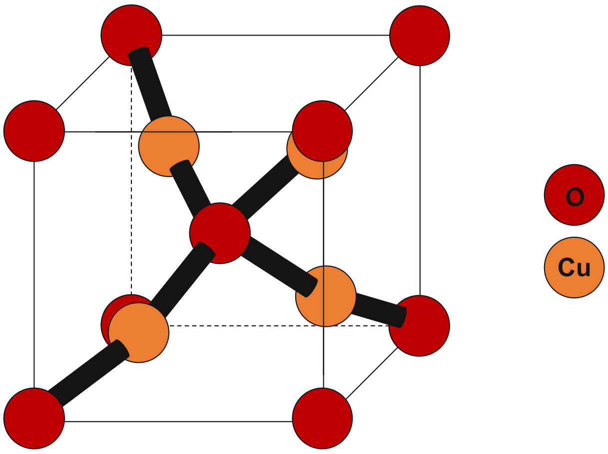

Figure 10: Crystal structure of Cu_2O

Table 2: Theoretical properties of cuprous oxide [58]

Compound formula	*Cu_2O*
Molecular weight (g/mol)	*143.09*
Melting point (°C)	*1235*
Density (g/cm³)	*6.0*
Unit cell	*cubic*

Cuprous oxide Cu_2O has been the absorber material of choice in this thesis for many reasons. Most importantly, it is a p-type semiconductor material providing an appropriate bandgap for water splitting. Its valence band lies at approximately -1,3 eV and the conductive band at +0,8 eV, which concludes a band gap of around 2.0 eV, depending on the literature. [59, 60]. Since it provides a direct band gap, more incident solar energy can be utilized without losses, compared an indirect bandgap. [60] So theoretically, a potential high enough to induce water splitting (≥1.23 eV) can be achieved, even considering the needed overpotential.

Cuprous oxide does not absorb solar energy along the entire UV-vis spectrum. The highest optical absorption coefficient α for thin films lies below a wavelength of around 500 nm. Then, the absorption efficiency decreases significantly until at 600 nm no more energy can be absorbed. [61] At approximately 600 nm, which is equivalent to 2.07 eV, the materials band gap has been reached. Cu_2O is an intrinsically p-type compound, making it suitable to use as a photocathode.

In terms of efficiency, it has been calculated, that Cu_2O photocathodes with a direct band gap of 2.0 eV can deliver photocurrents of up to 14.7 mA/cm², providing a theoretical solar cell efficiency of maximal 20 % in an AM 1.5 spectrum. [60] In reality, the highest power conversion efficiency achieved with an active layer made from cuprous oxide was at 8.1% with a MgF_2/Al-doped ZnO/$Zn_{0.38}Ge_{0.62}$-O/Cu_2O:Na p-n heterostructure. [62] Since we are regarding water splitting systems, the solar-to-hydrogen conversion efficiency is another important parameter. Recently, through combining Cu_2O with a hole transporting layer made from CuSCN, a remarkable STH efficiency of 4.55% has been reached within a PEC-PV tandem system. [38]

With cuprous oxide being an abundantly available material, it also brings economic and political benefits. In terms of fabrication processes, the material synthesis does not call for any acute toxic chemicals or sophisticated methods, increasing safety during production, as well as lowering the amount of hazardous waste. Furthermore, most commonly preparation methods for this material are relatively low in cost and do not necessarily require any sophisticated setup. [60, 63]

Compared to elemental copper, cuprous oxide shows poor corrosion resistance. [64] With its redox potentials lying within the band gap and within the water splitting half reaction's potentials, self-oxidation and self-reduction processes are very common (Figure 11). This concludes in it being low in stability in aqueous media, which is one of the main challenges in producing highly efficient PECs made from this material. [17]

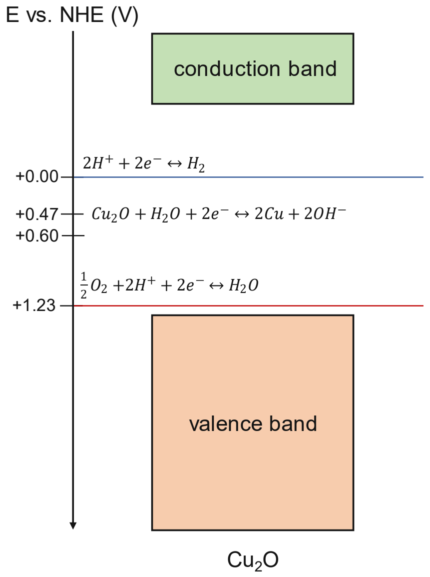

Figure 11: Energy band positions in Cu_2O in respect to the water splitting half reactions

Moreover, in electrodeposited Cu_2O minority carriers (electrons) have a diffusion length of approximately 10-100 nm [65]. At the same time, in the visible spectrum Cu_2O has a maximum absorption coefficient α of 10^5/cm at around 380 nm, which results in an absorption depth of 100 nm (α^{-1}). [66] Near the band gap, at around 600 nm, α lies only at around $3*10^4$/cm, as depicted in Figure 12. [61] With a corresponding absorption depth of 333 nm, electrodeposited cuprous oxide's minority carrier's diffusion length is too low to generate the maximum theoretical photocurrent. The increase of the carrier diffusion length can be achieved by reducing the amount of defects, increasing the grain size etc., thus achieving lower carrier recombination. However, this is a very difficult challenge. Taking into account the restricted diffusion length and the necessary thickness to achieve significant light absorption, a compromise must be found. As a result, thickness between 1-2 µm have been mostly used in the literature.

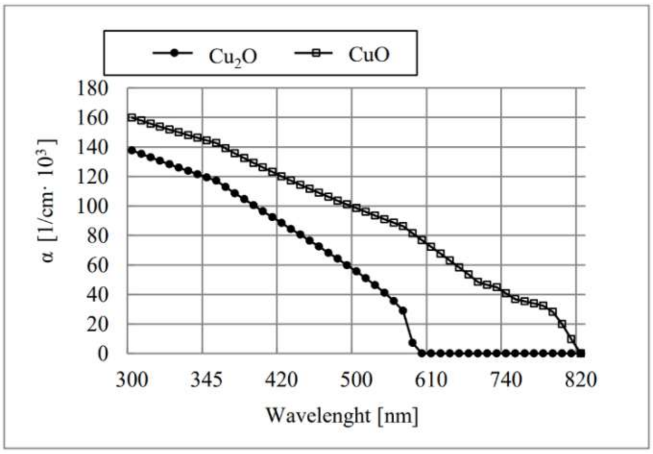

Figure 12: Absorption coefficient versus wavelength of Cu_2O and CuO [61]

3.3 n-type semiconductors

3.3.1 Zn(O,S), ZnO

In this thesis, n-ZnOS or n-ZnO are in direct contact with the absorber material, forming the p/n junction. The optical band gap of ZnO lies around 3.20 eV, whereas the band gap for ZnOS varies depending on the sulfur content, which is described by the band bowing parameters. This variation of the material's electrical and optical properties is caused by the great differences in sizes between O and S atoms. [67] By doping with sulfur, this zinc oxide alloy's CBM and VBM and therefore the overall band gap can be tuned (Figure 13). [67] The reported bandgap variation with O content x, is

$$Eg(x) = 3.6 - 0.4x - 3x(1-x)$$

for x=0 and x=1 Eg=3.6 eV (ZnS) and 3.2 eV (ZnO), respectively. [68] The bandgap minimizes when the S/O ratio is nearly 1 (Eg~3.0). The modification of the bandgap is the result of the continuous decrease of the conduction band minimum with increasing x, while the valence band maximum presents a maximum at x=0.5.

Additionally, ZnOS is an environmentally friendly and non-toxic candidate to use as buffer layer. [69] Previous studies have shown, that ZnO as buffer can improve photocurrent, as well as overall stability. However, the obtained onset potential was relatively low (~0.50 V vs. RHE), leading to low photovoltage. [40] The use of ZnS instead showed an increase of the onset potential to 0.72 V vs. RHE [40]. The use of the ZnOS compound has not been reported. In this thesis, the ZnOS films have the composition $ZnO_{57}S_{43}$ (as obtained by XPS measurements). The sputtered ZnOS films have an indirect bandgap of 2.83 eV and the wurtzite [002] texture, similar to ZnO.

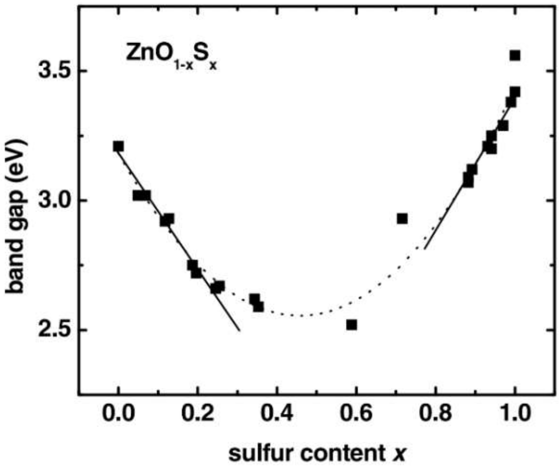

Figure 13: Band gap energy variations of $ZnO_{1-x}S_x$ *thin films dependent on their composition x [70]*

3.1.2 Niobium-doped Titanium oxide (NTO)

TiO_2 is an earth abundant material with different possible crystal lattice structures, such as anatase, rutile or mixture. [52] It has a large band gap between 3.0 and 3.5 eV [71]. By doping with transition metals, the material's properties can be adjusted. To decrease TiO_2's resistance, it can be doped with Niobium. Nb^{5+}'s radius is similar to Ti^{4+}'s, making it possible to be incorporated into the lattice and act as a donor. This results in electrons brought into the structure and therefore enhancing conductivity. However, the activation of the dopant usually involves thermal treatment. This makes NTO a doped n-type semiconductor. Another way to increase the conductivity of the material is by adding oxygen vacancies. [72] It has also been reported, that TiO_2 is stable over a wide range of pH and potentials and can therefore stabilize a PEC cell for 50 or more hours when providing a layer thickness of at least 40 nm prepared by ALD. [41] NTO therefore functions as a passivation layer, which protects the active semiconductor from degradation caused by harsh environmental conditions and corrosive electrolytes. Moreover, it has been reported, that TiO_2 can enhance electron transfer processes in water splitting systems. [40] Generally, the n-type NTO layer should be thick enough to cover and protect all the grains and guarantee a pinhole-free layer, but not too thick to eventually hinder charge carriers from transferring to the surface.

The sputtered NTO layers in this thesis are amorphous, with a Nb/Ti ration ~9%. The bandgap of the sputtered amorphous NTO is ~3.3 eV (indirect).

3.2 Co-catalyst

Since there are two types of reactions – HER and OER – necessary for water splitting, there are two kinds of approaches in terms of utilizing electrocatalysts. For the hydrogen evolution reaction, noble metals, largely Pt, Pd, Rh and Ru, seem to be the most active elements of choice. The OER on the other hand, can be enhanced using metal oxides, such as RuO_2, CoO or NiO. Despite lowering the reaction's overpotential needed for high current densities, those catalysts can also act as a protection layer against photocorrosion, which is a main issue of cuprous oxide. [11]

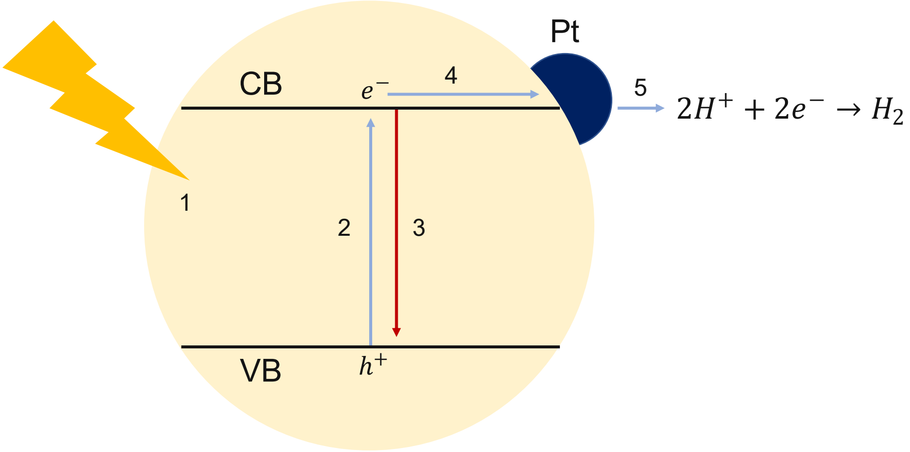

Figure 14: Working principle of a Pt HER catalyst

Figure 14 portrays the effect of co-catalyst in a Z-scheme photocatalytic water splitting device. The working principle: After light absorption (1) and excitation of a valence band's electron to the conductive band (2), the metal co-catalyst prevents e^-/h^+ recombination (3) through accelerating electron transfer (4) enabling quicker hydrogen production (5).

3.2.2 Platinum

Pt-based co-catalysts are widely used in the water splitting regime to enhance the hydrogen evolution reaction. They function as a low overpotential catalyst, which can prevent electrons from eventually being trapped, which might be an issue especially with NTO underneath. [17] Pt is a transition metal conductor with an electrical conductivity of 9.4×10^6 S/m. [73] Depositing Platinum in a pure and defect-free manner with good adhesion to the prior layer also strongly contributes to the co-catalyst's performance. [17] Its main drawback is it being a precious metal, hence costly and available in limited quantity, making it unrealistic to use in great amounts for commercialized purposes.

4. Electrochemical deposition (ECD) of Cu_2O

4.1 Preparation of the solution for the ECD of Cu_2O

To prepare the electrolyte solution for the electrodeposition process, 0.2 M Copper sulfate pentahydrate ($CuSO_4 \times 5H_2O$, Sigma C8027) were solved in 3 M lactic acid ($C_3H_6O_3$, Sigma, W261114) and stirred constantly in a water bath for cooling. Ultrapure milli-Q water (approximately half of the final total volume of 500 ml) was slowly added, and the solution was left stirring until all the salt has dissolved, which could take up to 4 hours. Then, highly concentrated NaOH solution (NaOH pellets, Sigma S5881, dissolved into the rest amount of the milli-Q water) was added to the mixture, decreasing the pH from an initial value of 0.7 to the final pH of 12.5. During this process, the water bath was replaced twice to ensure proper cooling. The final amount of NaOH was 3.5 M. At approx. pH 6-7, the pH value begins to change rapidly, as well the solution's color, which turns from blue to deep-blue and final to dark violet, with no precipitation observed in the solution. The solubility at this high pH is due to the fact that copper(II) ions are coordinatively bound to lactate ions. This prevents the formation and precipitation of $Cu(OH)_2$ that would hinder the deposition of Cu_2O. [74] The prepared solution was kept under constant stirring until it was thoroughly consumed, over a period of up to 1 week. Each time, an amount of ~150 ml was transferred from the stock solution to a beaker for the ECD of 3-6 samples, depending on the targeted thickness.

4.2 Substrate types and preparation

Prior to the ECD of Cu_2O all substrates underwent a cleaning procedure. Firstly, they were washed in ultrapure water with detergent (*Helmanex III*), secondly just in ultrapure water and thirdly in isopropanol. Each cleaning cycle was performed at 50°C in an ultrasonic bath, for 15 minutes. Afterwards, they were dried using a nitrogen gun. Right before using any of the substrates, each one was blown with the N_2 gun again, to ensure there is no dust or other particles on its surface.

A number of substrates were initially tested for the ECD of Cu_2O. However, two were selected for systematic investigations. The selected substrates fulfill two conditions: (i) they do not contain precious metals, and most particularly gold that is predominantly used in the literature as substrate for ECD-Cu_2O, and (ii) they lead to homogeneous Cu_2O film deposition due to a combination of electrical and structural properties. Specifically, the selected substrates were glass/ITO and stainless-steel foils, which are widely used in the industry for various optoelectronic devices, photovoltaics, and other applications.

Commercial glass/ITO substrates of 2.5×2.5 cm^2 area and 1 mm thickness (*Sigma Aldrich, CAS 50926-11-9*, with a sheet resistance of 8-12 Ω/sq.) were halved to ~2.5×1.25 cm^2 pieces using a glass cutting tool, whereas stainless steel foil substrates (100 µm thickness and sheet resistance of 7 mΩ/sq.) were cut using scissors to the same size of ~2.5×1.25 cm^2. The actual deposited area was ~1.8×1.5 cm^2 for each sample (2.25 cm^2).

4.3 Electrochemical deposition setup

The standard arrangement for all electrodeposition experiments consists of a three-electrode setup including the working (WE), counter (CE) and reference (RE) electrode. The working electrode is the conductive substrate on which the Cu_2O film is deposited. A Pt-coated steel mesh serves as counter electrode, whereas as reference, a Ag/AgCl electrode with a standard potential of $E_0 = 0.21\ V$ was used (from redox.me, with filling solution of KCl 3 M). The electrodes, connected to the AUTOLAB potentiostat, are placed in a 250 ml beaker filled with ~150 ml of the $CuSO_4$-solution and kept at a constant temperature of 60°C. For this, the beaker resides on a hot plate (CAT, MCS77). A temperature probe (thermocouple) is inserted in the solution and connected to the hotplate for the automated regulation of the solution temperature. During the deposition process the solution was not stirred, as stirring often caused inhomogeneous deposition over the substrate area (most probably due to a disturbed mass flow), reflected on non-stable chronoamperogram (CA). However, in-between the depositions, stirring was applied. The depositions took place in potentiostatic mode, *i.e.* the potential was kept constant at a defined value, whereas the current varied.

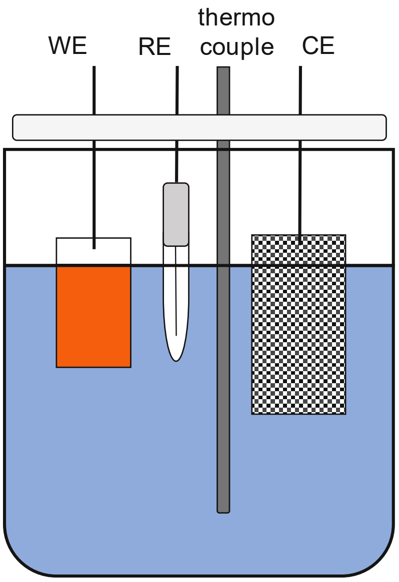

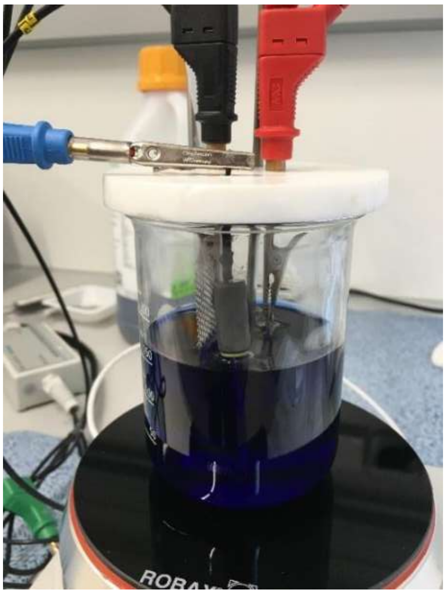

Figure 15: Scheme of the electrochemical deposition setup: the 3 electrodes (WE, CE and RE) and the thermocouple are immersed into the beaker filled with the deposition solution and connected to the potentiostat and the hot place, respectively.

Figure 16: Photo of the 3-electrode ECD setup. WE and CE are placed vis-à-vis with the side of the sample to be deposited facing the CE. RE and thermocouple are place in between.

4.4 Description of the electrochemical reactions

When electrodepositing Cu_2O thin films onto the working electrode, there are three possible electrochemical reactions occurring, two of which are pH-dependent. The targeted reaction is the formation of Cu_2O from Cu^{2+} ions and OH^- (reaction *XV*), which only occurs under alkaline conditions. At acidic pH, Cu_2O can be further reduced to elemental copper (reaction *XVI*), which should be prohibited. In alkaline environment (pH>7) Cu^{2+} solubility becomes very limited. To stabilize the Cu^{2+} ions in the deposition solution, lactic acid is used as a chelating agent. Free Cu^{2+} reacts with lactate ions $C_3H_5O_3^-$, forming the stable cupric lactate complex $Cu(CH_3CHOHCOO)_2$. This allows deposition at high pH [57]. According to the third reaction (reaction *XVII*) Cu^{2+} is directly reduced to metal Cu^0. [75] This reaction takes place at high applied anodic potential of around -0.79 V to -0.96 V vs. Ag/AgCl according to literature. [57, 76] This is why, applied bias of around -0.3 to -0.5 V have generally been chosen for depositing cuprous oxide, since within this region, its steady-state currents for Cu_2O bulk deposition align well with the material's LSV. [57] Studies have also shown, that Cu_2O structure switches from granular to cubic along with potential increase. Furthermore, the material's band gap energy changes with applied bias. Generally, band gap energy increases at higher anodic potential. [76] It is therefore clear that both the solution pH and the applied potential determine the chemical composition of the Cu_2O film and are very individual parameters.

$$2\,Cu^{2+} + 2OH^- + 2e^- \rightarrow \; Cu_2O + H_2O \qquad \text{(XV)}$$

$$Cu_2O + 2H^+ + 2e^- \rightarrow 2\,Cu + H_2O \qquad \text{(XVI)}$$

$$Cu^{2+} + 2e^- \rightarrow \; Cu \qquad \text{(XVII)}$$

4.5 Determination of the deposition potential

Prior to Cu_2O deposition, potentiostatic linear sweep voltammetry (LSV), from 0 V to -1 V vs. Ag/AgCl RE, was performed to determine the optimum deposition potential for the specific substrate. The applied potential determines the overall reaction kinetics and therefore the properties and characteristics of the deposited layer.

The relationship between the current density j and the activation overpotential η is described through the Butler-Volmer (BV) equation (IV). The activation overpotential is $\eta = E - E_{eq}$, with E_{eq}being the equilibrium potential, where the reduction and oxidation reactions at the electrode assume the same reaction rates. The reaction rate can be defined by product formed, or usually by ions consumed. For the latter, the flux of charge carriers involved from the bulk solution towards the cathode (inflow) need to be considered. At equilibrium $i_a = i_c = i_0$. This occurs, when anodic and cathodic polarization amount zero, which allows equation (*XIX*) to be reduced. [77] The exchange current density i_0 therefore is proportional to the forward and backward reaction at equilibrium. A low value would result in slow reaction kinetics, whereas high i_0 describe fast electrochemical reaction. [78]

$$i = i_0 \left(exp \frac{\alpha_{anodic} nF\eta}{RT} - \left[exp \frac{\alpha_{cathodic} nF\eta}{RT} \right] \right) \qquad \text{(XVIII)}$$

BV-equation describing the relation of electrode current density i (Acm^{-2}), along with exchange current density i_0, the charge transfer coefficient for the respective electrodes α, the number of electrons in the half reaction n and activation overpotential η

Considering Cu_2O deposition at the cathode, η_a is negative. Anodic polarization can be defined as

$$\eta_a = \beta_a log \frac{i_a}{i_0} \tag{XIX}$$

with β being the rate representing current density. Same goes for the cathodic regime respectively. [77] Furthermore, there is typically a great overpotential of $|\eta_a| > 100\ mV$, altogether resulting in the second term of equation *(XVIII)* being neglectable.

The dimensionless cathodic symmetry coefficient α can be derived from the slope of a linearly fitted linear sweep voltammogram. As shown in Figure 17, the slope of fit derived from deposition on glass/ITO amounts -7, which concludes a cathodic charge transfer coefficient of $\alpha = 0.20$, considering $slope = -\frac{\alpha F}{RT}$. Within that linear region, electrochemical reactions are charge-transfer-controlled – not diffusion-controlled, which shows, that reduced BV can only be applied within this regime. [79]

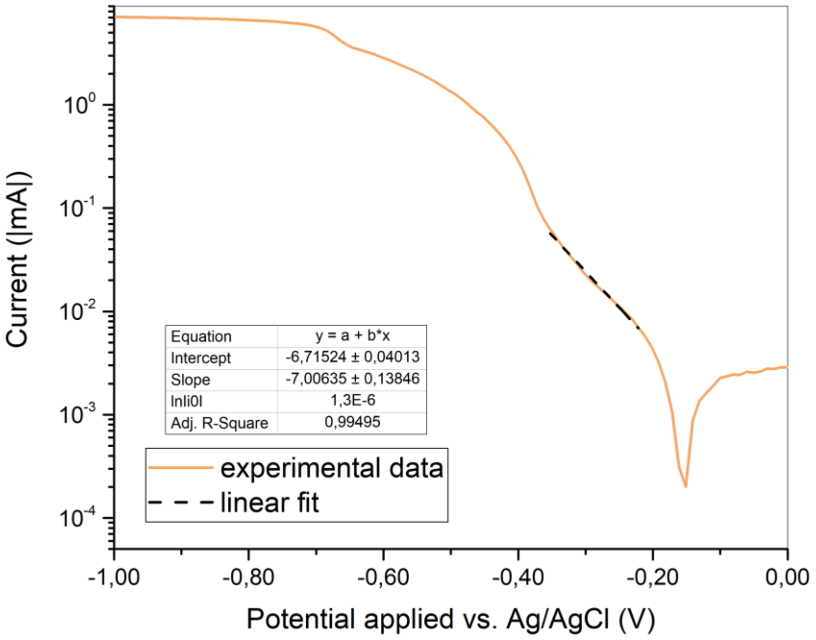

Figure 17: Linear fit of experimentally derived data of a linear sweep voltammogram using a glass/ITO substrate

The formation of thin films and nanostructures typically occurs through nucleation, followed by growth. Nuclei consist of atom clusters that form stable structures. In the case of electrochemical systems, nuclei form at the interface of electronically and ionically conducting phases, when changing the system's electric potential. [80] Their formation preferably takes place at low energy sites, such as a surface's active centers or surface defects. Starting from these nuclei, the growth process continues through incorporation of ions available in the surface's environment (electrolyte solution). These processes are based on charge transfer reactions. [80] In principle, the nucleation and growth processes can be divided into two regimes, depending on the applied potential:

- Charge-transfer-controlled
- Diffusion-controlled

If the rate of ions being formed into the new solid phase is the limiting factor, we are talking about charge-transfer controlled growth. Correspondingly, if the mass transport rate, at which ions from the solution migrate towards the electrode surface, determines the overall deposition, the growth is termed diffusion-controlled. [80]

The applied deposition potential has a determining effect on the layer's growth rate and consequently its morphology (including crystal texture, grain size and roughness). [81] The potential influences both the nucleation and growth regimes. Generally, with lower applied potential, the deposition process is charge-transfer-controlled, whereas with increased potential, the mass-transport-controlled regime eventually prevails. While the charge-transfer regime yields defect-poor layers, the growth rate is limited. On the other hand, the mass-transport-controlled regime yields high deposition rates but defect-rich deposits. The aim is to apply a deposition potential at the threshold between these two regimes to avoid defects, whilst achieving significant deposition rates.

Figure 18 schematically displays the effect of the deposition potential and the substrate's electrical conductivity on the deposition CAs. The general bell-shape of the curve is the result of an initial stage of nucleation and growth, where the electrode's surface area and therefore the current increases and eventually maximizes, followed by a second growth stage where the current gradually decreases concomitantly with the electrode's area, as the individual grains impinge on each other, and their lateral growth is sterically hindered. For a specific substrate, increased cathodic potential would lead to denser nucleation (with the current maximum obtained faster), resulting into smaller grains, smoother film morphologies and more structural defects. For two substrates of different conductivity the same applied potential would lead to faster nucleation and growth on the substrate with higher conductivity (Figure 18).

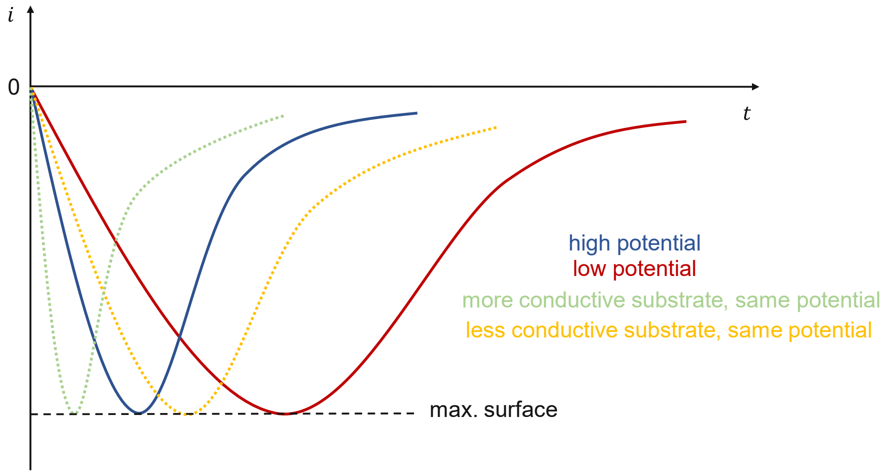

Figure 18: Comparing scheme of different ECD-rate's behavior dependent on bias applied and substrate chosen

Furthermore, there are two types of nucleation processes (Figure 21): The well-known Avrami scheme proposes that formed nuclei constantly increase in number. Besides, the nucleation formation is a multi-step process, which occurs randomly. Alongside the development of new nuclei, the existing ones grow isotopically. [82] This means, the availability of active sites for growing nuclei will vary along the process of covering the substrate and is also described as progressive nucleation scheme [80] Scharifker and Mostany (S-M) and further Scharifker and Hills (S-H) then considered the availability of a limited number of nuclei, all forming at the same time followed by gradual growth. [80] The S-M scheme can be applied for linear diffusion in plane diffusion zones [83, 84], proposing island growth being usually mass-transfer controlled (*Figure 19*). S-H then modified this model, also taking diffusion-controlled overlapping of hemispherical diffusion zones (*Figure 20*) into account. [85, 86] As seen in experimental results, the nucleation scheme undergone in these studies follows the Scharifker-Hills theory (red curve, Figure 21). Diffusion-controlled reaction schemes with hemispherical nuclei can be described by

$$i(t) = zFADc\left[\frac{1}{r_0} + \frac{1}{\sqrt{\pi Dt}}\right] \qquad \text{(XX)}$$

with zF being the charge transferred, A and r_0 describing the growth center's geometry, D the diffusion coefficient and c the to-be-deposited species' bulk concentration. [80] When maximal surface has been reached ($|i_{max}|$, black curve, Figure 21), current decreases as nuclei start growing, since i and A behave proportionally.

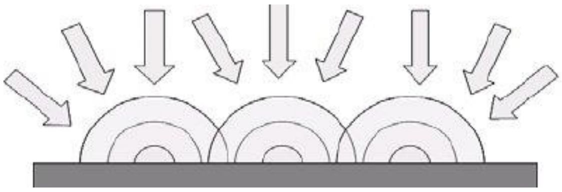

Figure 19: Hemispherical diffusion zones overlapping on the electrode surface [80]

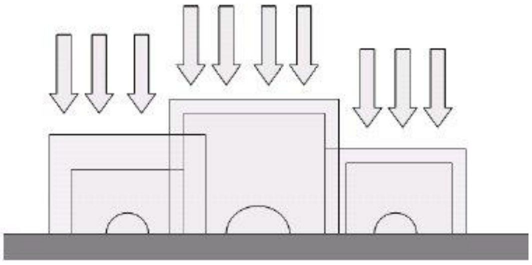

Figure 20: Planar diffusion zones overlapping on the electrode surface [80]

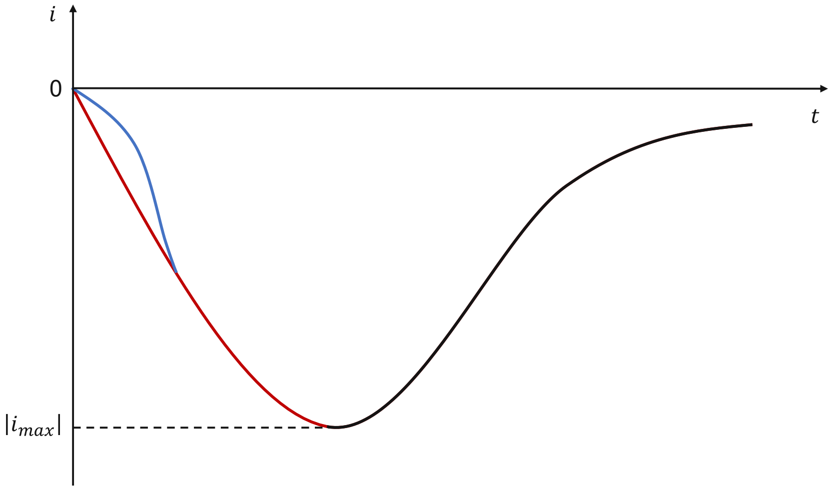

Figure 21: Avrami scheme (blue) and Scharifker-Hills scheme (red) describing two different nucleation and growth mechanisms

To decrease the possibility of holes in the film, which will eventually act as electrical shunts in the PEC device and degrade its performance, the deposition with a dual potential can be used: firstly, a lower deposition potential is used to achieve high nucleation density, smaller grains, and more compact morphology. Then a higher deposition potential is applied to decrease the number of structural defects and obtain higher quality interfaces with any additional layers that may be deposited on top of the Cu_2O.

The optimal deposition potential is derived from linear sweep voltammetry, expressing the measured i-V curve in a semi-logarithmic scale.

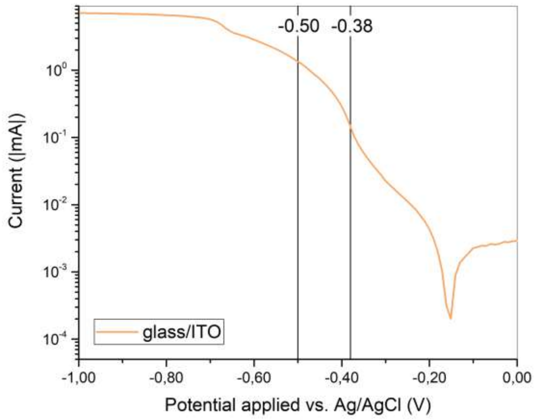

Figure 22: Potential-current dependency of Cu_2O-ECD from a $CuSO_4$-solution with pH=12.5 on a glass/ITO substrate at 60°C

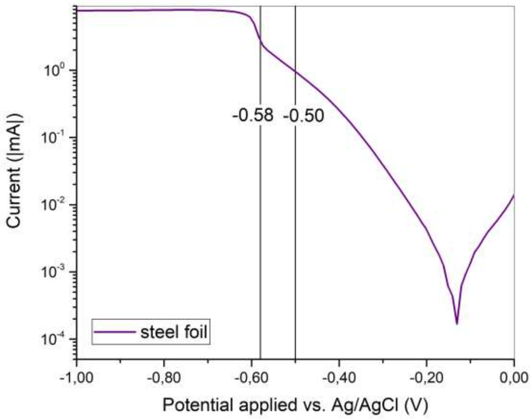

Figure 23: Potential-current dependency of Cu_2O-ECD from a $CuSO_4$-solution with pH=12.5 on a stainless-steel substrate at 60°C

The aim is to choose a deposition potential as low as possible, but still within the linear regime of the LSV curve. This would mean, the reaction is at the threshold between the diffusion-controlled and charge-transfer-controlled regimes, as described earlier. With glass/ITO substrates (*Figure 22*) it has been proven to be useful to increase the set potential from 0.45 V to 0.57 V vs. RHE after half the reaction's current flow has taken place. For samples deposited on steel foil (*Figure 23*), experiments executed at 0.37 V or 0.45 V vs. RHE were compared and concluded that a set potential of 0.45 V vs. RHE yields layers of higher quality.

4.6 Potentiostatic deposition of Cu_2O

The targeted Cu_2O thickness was 2.5 µm, chosen as a compromise between achieving adequate light absorption and efficient photogenerated charge-carrier extraction (see discussion in 1.3.1). In the literature, thicknesses in the range 0.18 [47] to 4.7 [48] µm have been employed.

In the electrochemical deposition, the thickness can be monitored and determined through the total charge that has flown in the cell over time, according to Eq. *XXI* (Faraday's law)

$$Q = \frac{\rho\, d\, n\, F\, A}{M} \qquad \text{(XXI)}$$

where Q is the charge in Cb, ρ is the density of Cu_2O (6 gcm^{-3}), d the thickness, n the transferred electrons per electrochemical reaction (n=2), F is the Faraday constant (96485.33 $Cmol^{-1}$), A the deposited area in cm^2 and M the molecular weight (143.09 $gmol^{-1}$).

For the targeted thickness of 2.5 µm and A=2.25 cm^2, the charge equals to Q = -4.55 Cb. Upon reaching this charge value, the deposition was stopped, the sample taken out of the bath, washed in flowing DI water, and then dried with a N_2 gun.

4.6.1 Deposition and characterization of Cu_2O on glass/ITO

For the initial deposition on glass/ITO substrates, a potential of -0.38 V vs. Ag/AgCl (+0.57 V vs. RHE) was chosen. Due to inhomogeneity in the resulting layer, which is also noticeable in the I-t curve's form (*Figure 24*), it was decided to divide the deposition process into two segments with different applied potentials. Firstly, a larger potential of -0.50 V vs. Ag/AgCl (+0.45 V vs. RHE) was chosen to enhance the nucleation density. The process was stopped after depositing around half of the Cu_2O layer until a charge of -2.2 C has flown, which equals a thickness of 1,21 nm. Following, the potential of -0.38 V vs. Ag/AgCl was applied for the remaining thickness (corresponding to -2.35 C). This slower rate ensures a defect-poor film.

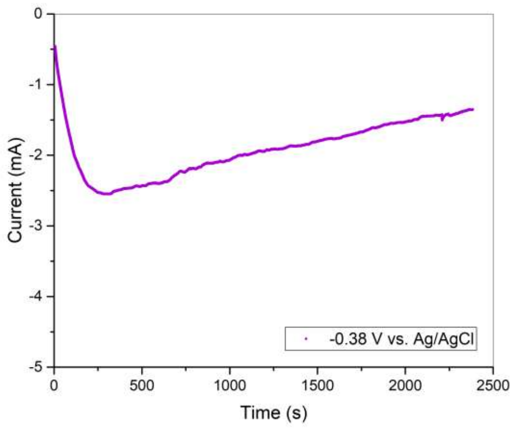

Figure 24: ECD of Cu_2O on glass/ITO with a constant applied bias of -0.38 V vs. Ag/AgCl

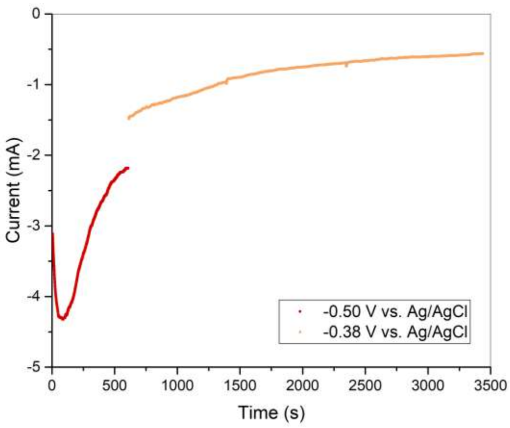

Figure 25: ECD of Cu_2O on glass/ITO with an initial applied bias of -0.50 V, followed by -0.38 V vs. Ag/AgCl

As for the result, the samples produced using this "dual-potential" approach showed a more homogeneous deposition (Figure 25), combined with vibrant color (Figure 26) that is due to a higher packing density and smaller grains. These samples showed also increased performance in electrochemical testing. The only downside arising when comparing the procedure displayed in Figure 24 to Figure 25, is the increased depositing duration from around 40 minutes up to 1 hour.

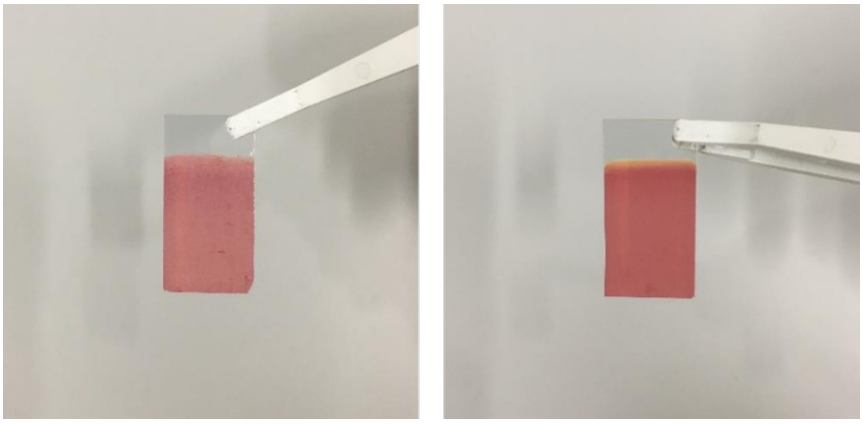

Figure 26: Cu_2O layer deposited without (l.) and with (r.) dual-potential approach

Figure 26 displays cross-section and top-view SEM images of the as-deposited Cu_2O films. The cross-section images show that the expected thickness from the total charge flow during deposition agrees with the actual layer thickness (~2.4 µm). Furthermore, the homogeneity of the Cu_2O throughout the entire layer is visible. Regarding the top-view images, the crystals are highly faceted, without large-scale defects and size in the range of few micrometers. Their form is representative to a cubic crystal structure, the texture of which will be later investigated by XRD.

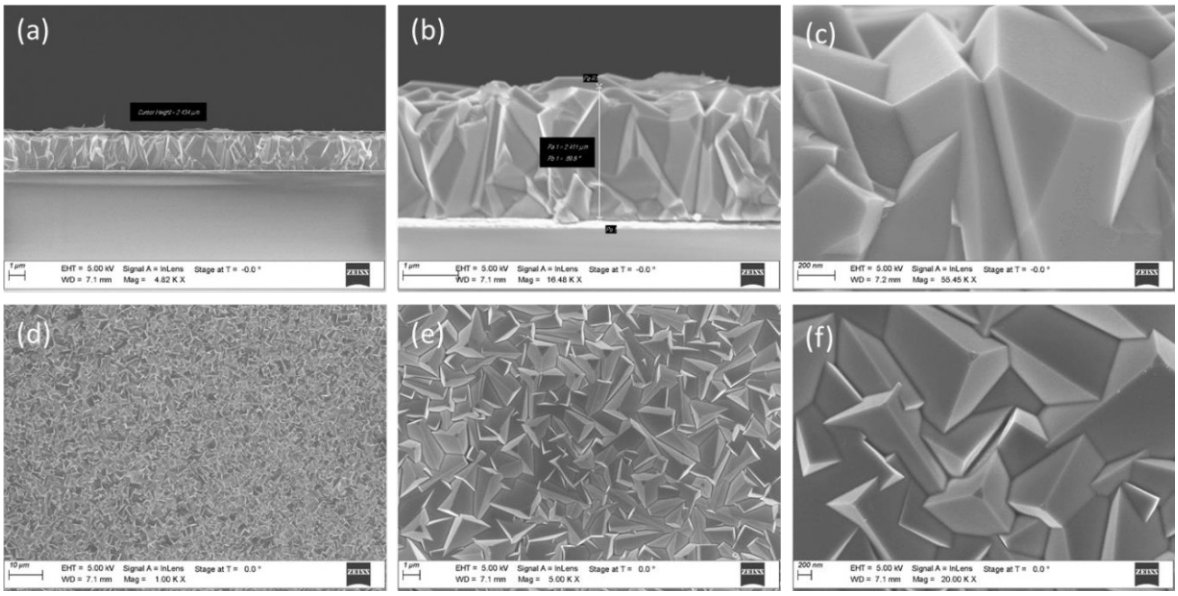

Figure 10: (a)-(c) Cross section SEM images of increasing magnification of a glass/ITO/Cu_2O sample deposited with a dual potential. The layer thickness is ~2.4 µm (d)-(f). Top-view SEM images of increasing magnification of the same sample.

The dual-potential-deposited layer of cuprous oxide on glass/ITO substrate was characterized using x-ray diffractometry. Figure 27 displays a diffractogram measured at an angle of ω=2°, along with a reference pattern for cuprite (reference card no. 96-101-0927). The reference aligns very well with the experimentally derived data with Cu_2O's characteristic peaks at emergent angles 2θ of 36.6, 42.5, 61.7 and 73.9 degrees.

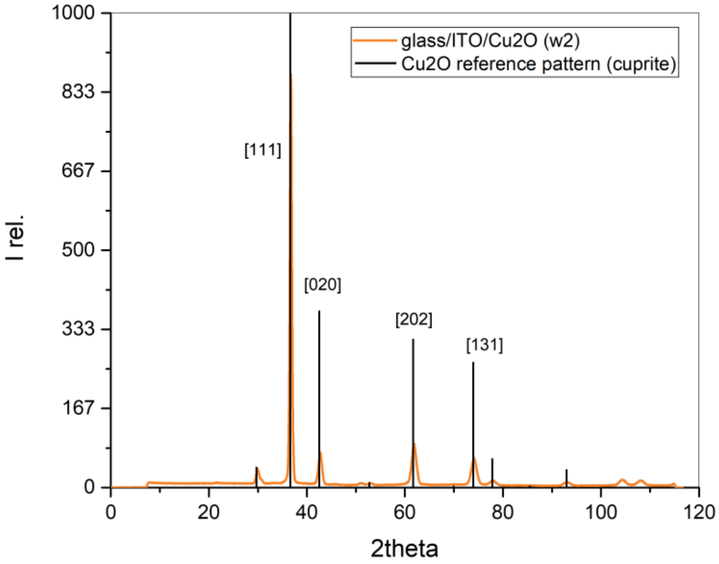

Figure 27: X-ray diffractogram of cuprous oxide deposited on glass/ITO measure at sample angle of ω=2°

Cuprous oxide's main peaks appear to be low-index facets, meaning the sum of their Miller indices is rather low. Typically, low-index facets mean lower surface energy, resulting in slower crystal growth. Consequently, this leads to greater density of atoms, making the final structure more compact and overall having the initial structure preserved in the final orientation. [87] In the case of [111] Cu_2O, some Cu-atoms are under-coordinated. In its unit cell, every Cu binds two neighboring O-atoms, resulting in electric neutrality. With unsaturated Cu-atoms, more precisely every second atom having one dangling bond, positive charge is possible (Figure 28). These charges can then interact with negatively charged atoms, resulting in greater crystal surface stability. Literature has shown, that [111] *o*-Cu_2O provides greater photocatalytic activity than *f.e.* [100] *c*-Cu_2O, due to the latter not being positively charged. Higher facet structures appear to show even further improved activity. [87]

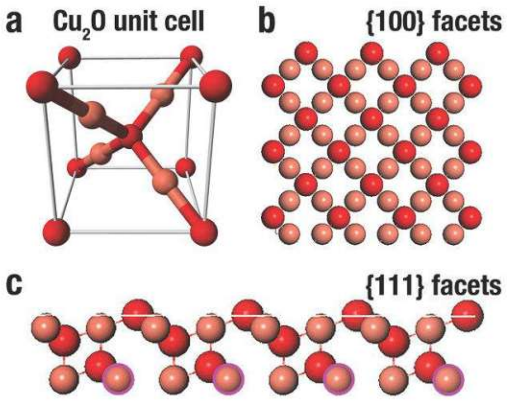

Figure 28: Cu$_2$O unit cell (a), electrically neutral (100) facet (b), positively charged (111) facet (c) [87]

4.6.2 Deposition and characterization of Cu$_2$O on steel foil

Based on the corresponding LSV, a potential of -0.58 V vs. Ag/AgCl was chosen for the ECD of Cu$_2$O on the steel foil. Nevertheless, after investigating the resulting chronoamperometry curve, it was decided, that this value is too high to provide conditions for high-quality deposition, with well-defined nucleation and crystal growth regimes, as shown in Figure 29. Changing the applied potential to -0.50 V vs. Ag/AgCl helped eliminating this problem. As seen in Figure 29, the deposition curve reflected well-defined growth, but the deposition duration was ~3-4 times longer at this potential. It is also important to note, that for the desired layer thickness of 2.5 µm, twice the amount of charge (*i.e.* -9.1 Cb) is necessary since the foil is conductive from both sides and therefore the Cu$_2$O is deposited on both sides of the substrate.

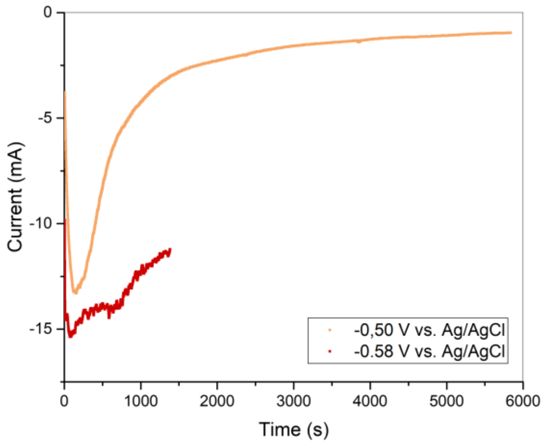

Figure 29: ECD current-time curve at different potentials on steel foil

Figure 30: Cu$_2$O electrodeposited on stainless-steel foil at -0.50 V vs. Ag/AgCl

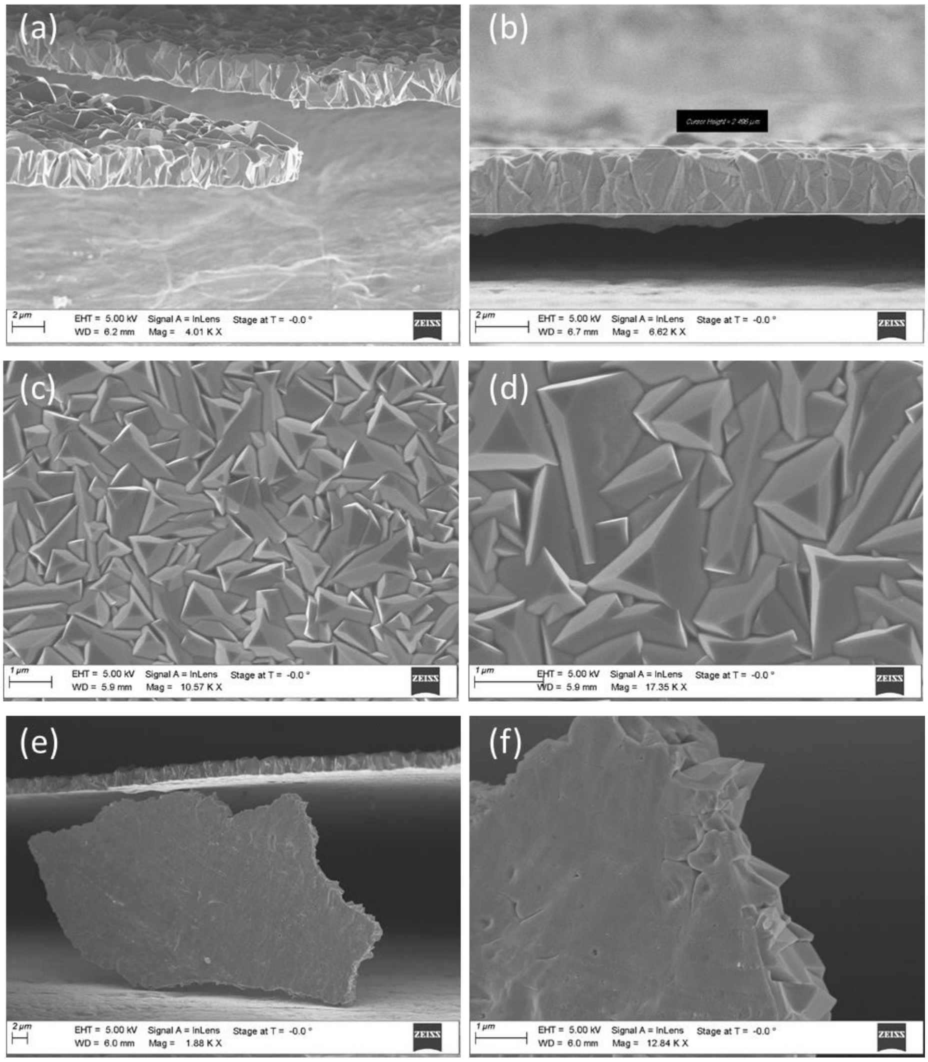

Figure 31: (a), (b): Cross sections of the Cu_2O layer on the steel substrate, showing a layer thickness of ~2.5 µm. (c), (d): Top view of the Cu_2O layer, showing closely-packed crystals, with morphology and size similar to what obtained for the glass/ITO substrate. (e), (f): Views of the back-side of the delaminated Cu_2O layer (that was formally in contact with the steel substrate), verifying the closely-backed layer morphology.

Figure 13 shows SEM images of cross sections and top views of the Cu_2O layers on the steel foil. To acquire these images, the surface of the sample was scratched with a sharp cutting tool. By observing the sample from an oblique angle, it was possible to find regions were the layer remained undamaged, as well as regions where the layer delaminated from the steel substrate. That also rendered it possible to have images from the back side of the delaminated Cu_2O layer (that was initially in contact with the steel substrate). This enabled a depiction of a cross-sectional (a, b), top- (c, d), as well as bottom-view (e, f) of the sample (Figure 31). In terms of homogeneity, layer thickness and crystal size, layers deposited on steel are similar to those on glass/ITO.

Analog to Cu_2O deposited on glass/ITO, samples based on steel foil were measured using XRD. The reference pattern of cuprite also aligns perfectly with the experimental data (Figure 32).

This concludes that cuprous oxide with identical crystal structure can be deposited on glass/ITO, as well as steel using the same electrochemical depositing procedure.

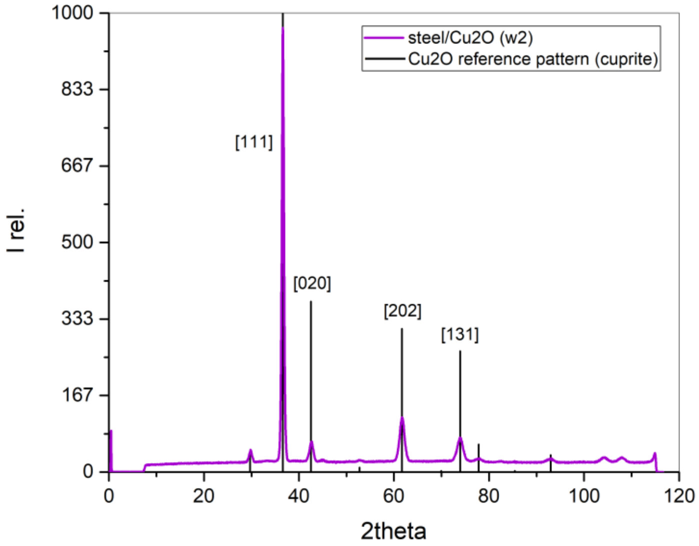

Figure 32: X-ray diffractogram of cuprous oxide deposited on steel measure at sample angle of ω=2°

In the literature it is proposed that in strongly alkaline environment, at a potential of -0.4 to -0.45 V electrodeposited cuprous oxide tends to form [111] oriented crystals on stainless-steel. [88] Depositions at lower (9) and higher (12) pH values in relation to the type of ligand used were distinguished. When looking at Cu-H_2O's Pourbaix diagram (Figure 33), it shows, that Cu_2O is only stable at negative potential at a pH of >8. Nevertheless, with increasing pH, $Cu(OH)_2$ might form as well.

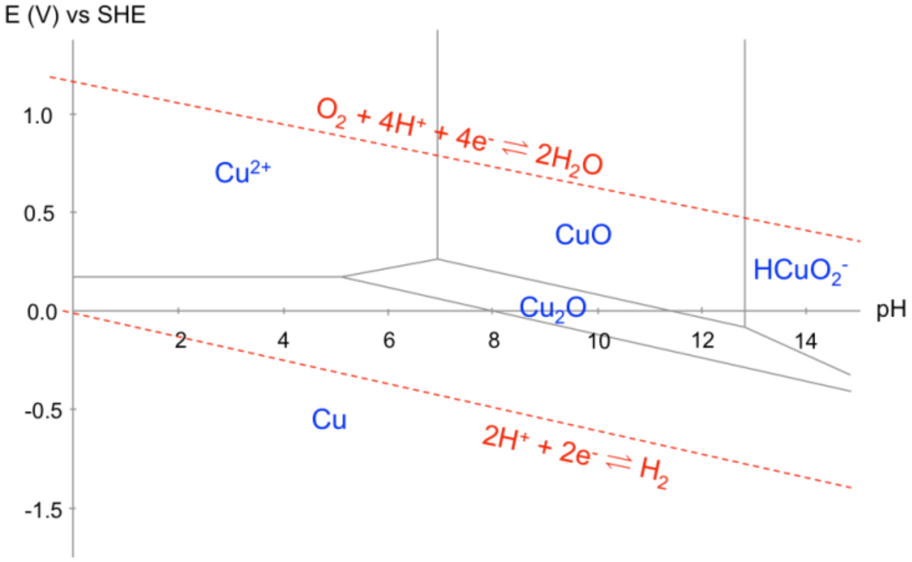

Figure 33: Pourbaix diagram of a copper-water system [89]

The formation of [100] facets, which show lower O^{2-} density, are preferably obtained at lower pH values. Respectively [111] oriented structures with more oxygen ions per unit rather form at higher pH. [88] This is because higher pH results in faster nucleation, leading to higher nuclei density. [65] This explains the strong tendency towards [111] orientation and absence in [100] when using lactic acid as complexing agent, as shown in Figure 32.

4.7 Sputter deposition of window and co-catalyst layers

For depositing the window and co-catalyst layers, sputtering was the applied technique. With this physical deposition method, the deposition chamber is being evacuated to high vacuum (HV). Afterwards, the chamber is filled with an inert sputtering gas – in this case Argon.

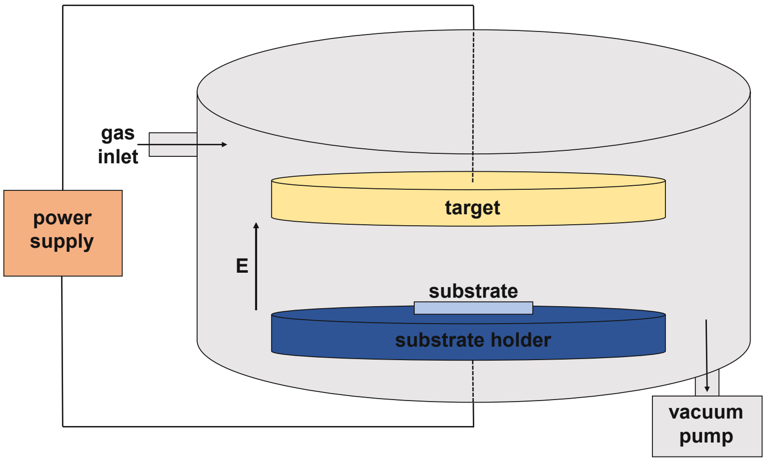

Figure 34: General setup of a sputtering device

When high negative voltage is applied to the source, which the sputter target is attached to, plasma generation is initiated. As depicted in Figure 35, electrons are accelerated towards the positively charged substrate (anode). On their way, they collide with Ar, leading to the ionization of Ar to Ar^+. The cations then are accelerated towards the negatively-biased target (cathode). The cations bombard the target and extract material from it, which is then is deposited on the substrate. This bombardment generates heat, which is why a water-cooling system of the target is required. During the target bombardment electrons are also extracted from the target, called secondary electrons, which are accelerated in the electric field towards the anode and in their way ionize more Ar, thus sustaining the plasma. To concentrate the secondary electrons at close proximity to the target, an array of magnets is placed behind the target creating a magnetic field that "traps" the electrons at the proximity of the target's surface, increasing the Ar ionizations.

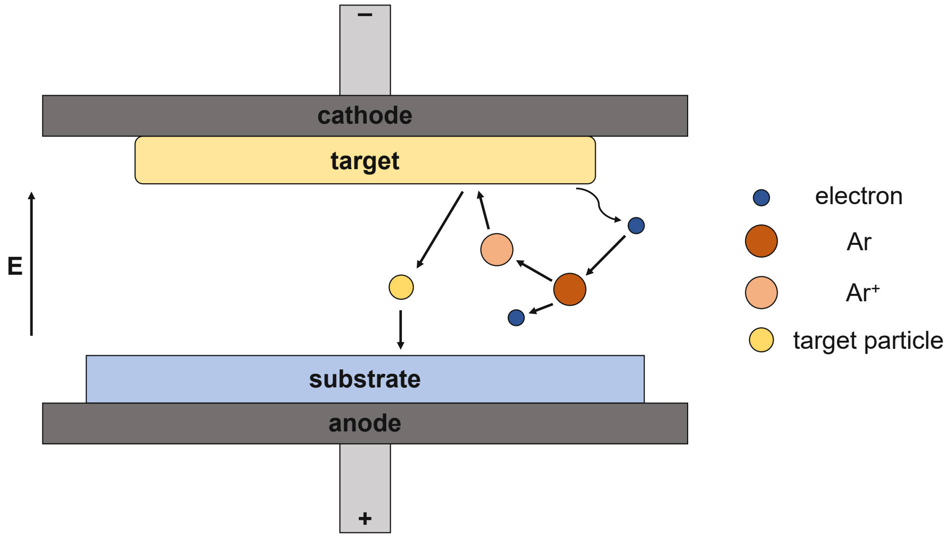

Figure 35: Working principle of DC sputtering

With non-reactive sputtering, only inert gas is present into the chambers, whilst with reactive sputtering, other gases (typically oxygen to create oxides, or nitrogen for nitrides) are introduced as well, to react with target ions before reaching the substrate. [90] The sputter sources are either supplied by DC (direct current) or RF (radio frequency) power. DC power is the most commonly used, since it leads to higher sputter rates. Hereby, a constant negative potential is applied to the target. A DC supply is suitable for metallic and semiconducting targets, as it requires that the target is electrically conductive. For insulating target materials, RF power is required. The application of a DC power in this case would soon charge the target's surface positively and eventually stop the plasma. By using RF power (with a frequency of 13.56 MHz), this is avoided. [91] Within each cycle, when negative voltage is applied, Ar^+ collides with the target, whereas when positive voltage is applied, electrons are accelerated to the target neutralizing the built-up charge. Sputtering is a widely industrialized technique. The main advantages of the sputtering technique lie in it allowing control concerning the deposited layer thickness, providing deposition with low probability of contamination due to HV and automatization of the process.

4.8 Sputter deposition of ZnOS and NTO layers

Depending on the target and desired layer thickness, the sputtering processes parameters varied, as displayed in Table 3. All samples were deposited in Argon inert gas atmosphere. The deposition chamber had a base pressure of $1.2x10^{-7}$ mbar. The samples were transferred from the load lock to the deposition chamber when the load lock reached $1x10^{-6}$ mbar. Using Kapton® tape, the samples were hold onto the sample holder to ensure an even surface, as well as to protect part of their conductive area from completely being covered (Figure 36). The deposition pressure and power are shown in the following table.

Table 3: Standard settings for sputtering window layers

Target	Modus	Pressure (µbar)	Power (W)	Time (s)	Thickness (nm)
$ZnO_{60}S_{40}$	RF	5	100	287	50
$Nb:TiO_2$ (NTO) (5 at.% Nb)	DC	5	120	382	50
$Nb:TiO_2$ (NTO) (5 at.% Nb)	DC	5	120	764	100

Figure 36 shows cuprous oxide deposited on glass/ITO (top) and steel foil (bottom) with a sputtered layer of zinc oxysulfide, followed by niobium doped titanium oxide. The variation in color in the top two samples comes from difference in layer thickness of Cu_2O, since in a) it amounts 2.5 µm and in b) 4.45 µm. As for c) and d), the absorber layer thicknesses are 2.5 µm and 3.45 µm respectively. The thin films of ZnOS and NTO amount for all four samples 50 nm each.

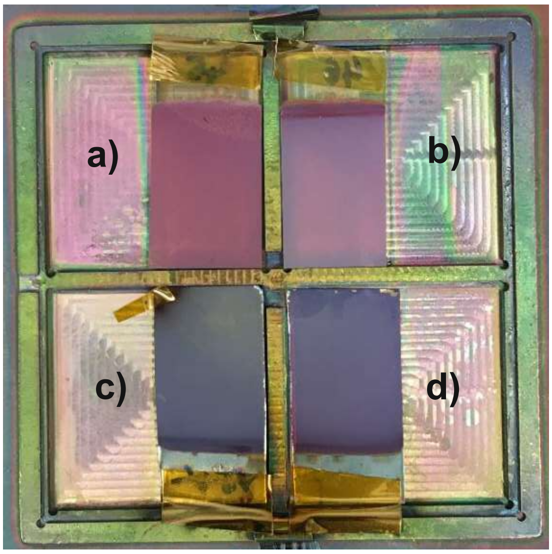

Figure 36: Samples with varying absorber layer thickness on a sample holder fixed with Kapton® tape a),b): glass/ITO/Cu_2O/ZnOS/NTO c),d): steel/Cu_2O/ZnOS/NTO

4.9 Sputter deposition of co-catalyst layers

The platinum co-catalyst was deposited under the parameters shown in Table 4. For some samples an aluminum shadow mask was applied prior to Pt-deposition, to cover only parts of the sample with the co-catalyst (Figure 37). In this case we wanted to avoid the creation of electrical shunts at the sample's edges after the Pt deposition. Two different kinds of masks were used: One as shown in the photo and another rectangular one as schematically illustrated (Figure 37).

Table 4: Standard settings for sputtering co-catalyst layers

Target	Modus	Pressure (µbar)	Power (W)	Time (s)	Thickness (nm)
Pt	DC	5	20	16	3

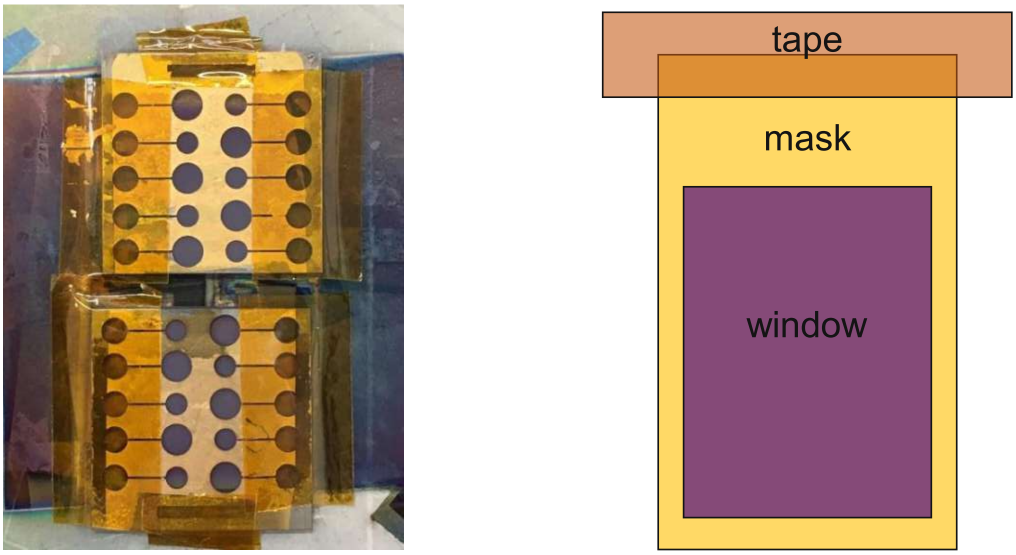

Figure 37: Samples on glass/ITO after depositing Pt under the usage of a partially covering flexible mask

5. Results and discussion

5.1 Electrochemical analysis

In the majority of experiments, we used the conditions displayed in Table 5. When different conditions were used, these are mentioned in the respective graphs. All samples were tested under chopped illumination (light intensity 100 mA/cm^2, AM 1.5G spectrum), by means of linear-sweep voltammetry, to probe the dependence of the (photo)current as a function of the applied potential, and chrono-amperometry, to test the stability of the photocurrent over long durations. Ideally, there should be minimal current when there is no illumination (dark current). On the contrary, the aim is to achieve high current density under illumination, while preventing the degradation of the photoelectrode. This means that the charge carriers are used to realize the HER and not for the chemical modification of the photoelectrode itself. Through equation XXII we can convert the potential vs Ag/AgCl ($E_{Ag/AgCl}$) electrode to potential vs RHE (E_{RHE}), considering the reference electrode potential (E_{RE}) and the pH of the solution.

$$E_{RHE} = E_{Ag/AgCl} + 0.059 \times pH + E_{RE} \tag{XXII}$$

Table 5: Used conditions for the electrochemical testing in the majority of experiments

Working electrode (WE)	Photocathode (sample)
Counter electrode (CE)	Platinum mesh anode
Reference electrode (RE)	Ag/AgCl E_0=0.21 V (*redox.me*)
Electrolyte	1 M Na_2SO_4 (pH=3)
Container	250 ml Duran® beaker
Irradiation	AM 1.5 1 sun (1 kW/m^2) front illumination
Illuminated area	Circular, d=0.5 cm, A=0.2 cm^2
Stirring	no
Nitrogen purging	no

5.1.1 Linear-sweep voltammetry – onset potential

In a particular window of applied potential, a cell's photocurrent density and energy conversion efficiency are optimized. This potential window is different for each sample and type of electrolyte. The optimal potential for maximum current density is derived from the sample's linear-sweep voltammogram (LSV). Another important parameter extracted from the LSV, is the onset potential. This can be defined as the potential where the current passes from positive (anodic current) to negative (cathodic) values (potential for I = 0 A). Usually, with bare Cu_2O absorber layers, thus forming an absorber/electrolyte junction, this potential (versus

RHE) is positive and in the range of some millivolts to several hundreds of millivolts. The use of the buffer and passivation layers, with the creation of a buried, solid-state, p-n junction, results in an improved carrier separation and transport and thus to an additional photovoltage, which shifts the onset potential to more positive values. Since we are working with photocathodes, the optimal applied potential is always more negative than the onset potential (to obtain cathodic current). Figure 38 shows a schematic i-V curve, illustrating the optimum potential that maximizes the photocurrent, as well as the onset potential.

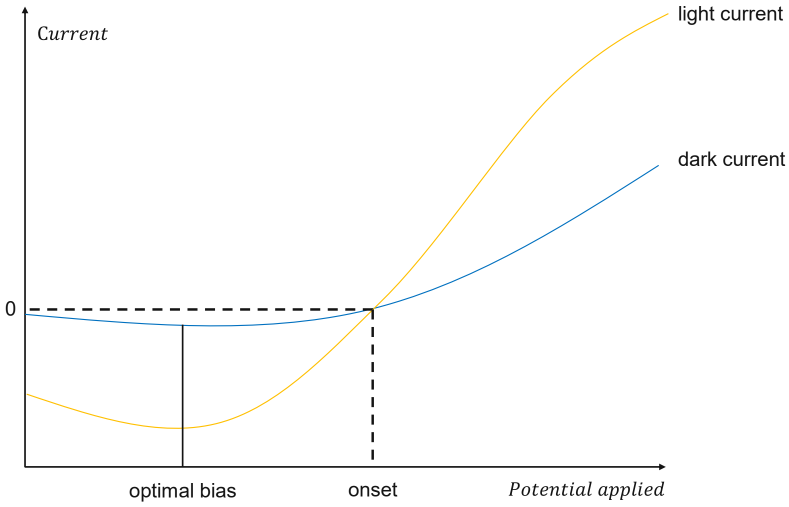

Figure 38: Schematic illustration of a linear sweep voltammogram to determine a sample's onset potential and ideal applied bias for maximal photo current

The maximum onset potential achieved for bare cuprous oxide on glass/ITO amounts +0.45 V_{RHE} at the experimental conditions of Table 5. With the deposition of the buffer and passivation layer on top, there is a shift of the onset potential towards more positive values noticeable. This shift can vary depending on the window layers. For the ZnOS/NTO window layers, the shift is 0.13 V (Figure 39), resulting in an onset potential of >0.5 V_{RHE}. If we compare the same pair of samples on the steel substrate, we see that the deposition of the window layers does not alter the onset potential, which is ~0.62 V_{RHE} (Figure 40). This shows that the gain in onset potential with the use of window layers depends on the absorber properties and interface quality. As general observation, the applied window layers improved the observed onset potential values. However, the reproducibility of these high onset potentials was limited, which underlines the challenging task of the multilayer deposition and the accurate control of interface quality.

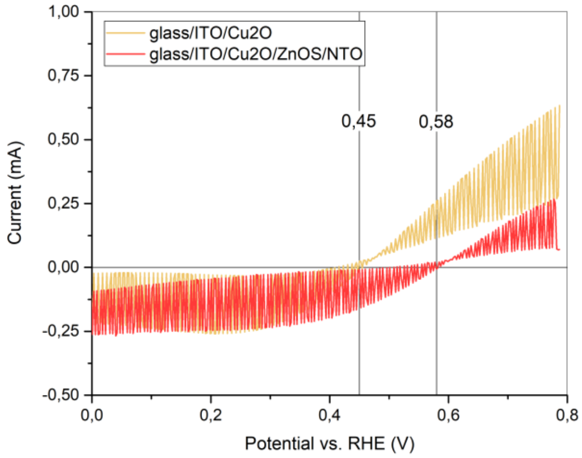

Figure 39: Linear sweep voltammogram: Effect of ZnOS/NTO window layer on top of glass/ITO/Cu_2O on the onset potential

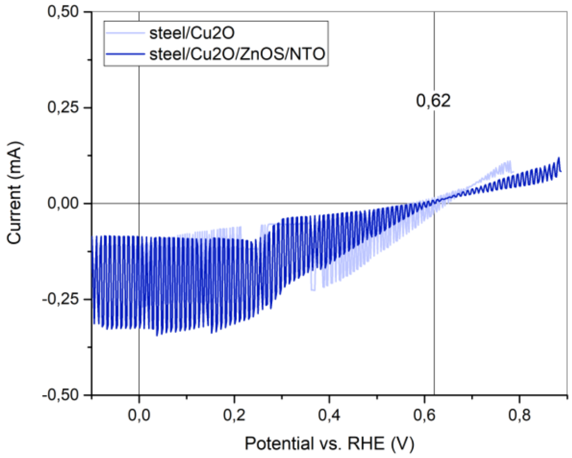

Figure 40: Linear sweep voltammogram: Effect of ZnOS/NTO window layer on top of steel/Cu_2O on the onset potential

Generally, samples deposited on steel have more positive onset potential compared to those based on glass/ITO. Regarding the optimal potential for maximum current density, potential lower than 0.4 V_{RHE} are preferable. For the majority of glass/ITO-based samples, as well as for the steel-based ones, applying a bias of 0 V_{RHE} (-0.39 $V_{Ag/AgCl}$) is most beneficial. This tendency has especially been confirmed with the photocathode's stability tests using chronoamperometry (5.1.2).

5.1.2 Stability of the photocurrent density

5.1.2.1 General performance of glass/ITO and steel-based samples

In the following discussion, with *current density j* we describe the difference of the measured light (j_{light}) and dark (j_{dark}) current density ($j=j_{light}-j_{dark}$). The current flow is due to the HER at the cathode/electrolyte interface, but also due to the photocathode degradation (e.g. oxidation of the photocathode from Cu_2O to CuO). These two contributions cannot be separated unless the total amount of H_2 produced is measured. However, this was not possible in the framework of this work.

Photocathodes with bare absorber (no additional window or catalyst layer) showed the highest current density. With applied potential of 0 V_{RHE}, a current density of up to $j = 2.15\ mA/cm^2$ has been achieved on glass/ITO-based cells, as shown in Figure 41. Due to the absorber layer not being protected from the highly acidic electrolyte (pH=3), this amount of current is not sustainable and fastly decreases, as the photoelectrode degrades. With same applied potential but using a less acidic electrolyte solution (pH=6), the degradation is delayed, but the maximum current density reaches $j = 0.65\ mA/cm^2$.

Generally, when more positive potential values are applied, they result in a shift of light and dark current towards more positive values (as also shown in the LSV curves). As shown in Figure 42 and 43, in the case of applied potential of +0.39 V_{RHE} (0 $V_{Ag/AgCl}$ in an electrolyte of pH=3), this can result in anodic currents (Figure 42, Figure 43), for samples with bare Cu_2O absorber, with reduced onset potential. However, at the same potential, the currents turn to cathodic for samples employing window layers, due to the positive shift of the onset potential (see discussion in the previous paragraph).

Since the glass/ITO substrate is highly transparent, it also allows to test the effect of front- (layer-side) and back (substrate-side) illumination on the photocurrent density. It was observed that the overall performance concerning measured current density is poorer when the sample is being illuminated from the back-side. One of the reasons is the larger light absorption due to the glass substrate. Another reason is that front-side illumination leads to higher energy UV light being absorbed close to the heterojunction, where the charge carrier separation is most efficient. However, the two experiments conclude same stability, regardless of which sample side is facing the lamp.

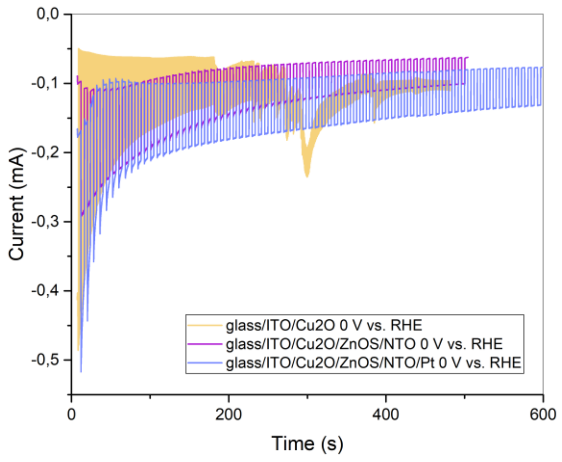

Figure 41: Stability test of bare Cu_2O (yellow), with window layer (purple) and with co-catalyst (blue) on glass/ITO at 0 V applied bias vs. RHE

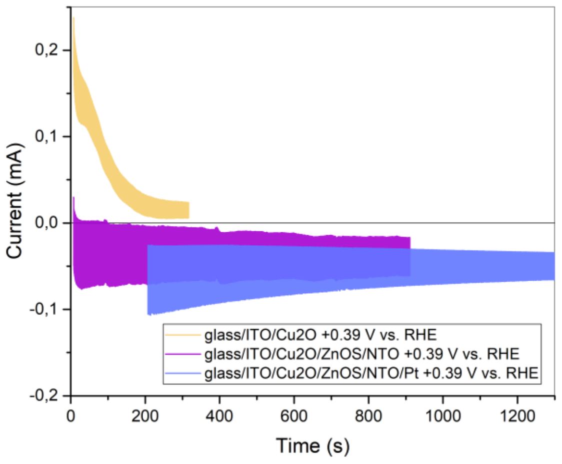

Figure 42: Stability test of bare Cu_2O (yellow), with window layer (purple) and with co-catalyst (blue) on glass/ITO at +0.39 V applied bias vs. RHE

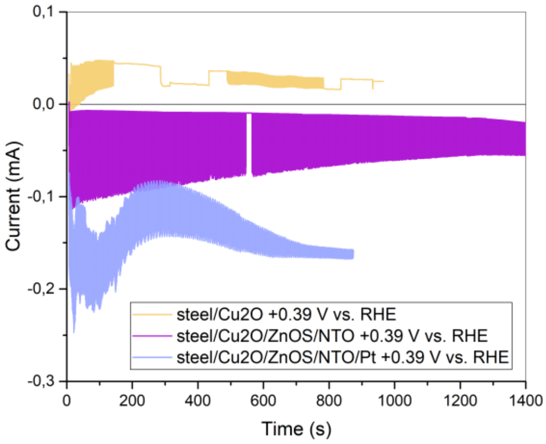

Figure 43: Stability test of bare Cu_2O (yellow), with window layer (purple) and with co-catalyst (blue) on steel at +0.39 V applied potential vs. RHE

5.1.2.2 **Effect of applied potential on current and stability**

Investigating photocathodes with additional buffer (50 nm of ZnO or ZnOS) and passivation (50 nm NTO) layers, a significant shift of current towards the negative (cathodic) realm for measurements executed at +0.39 V_{RHE} was observed, as shown in Figure 45, compared to experiments performed at 0 V_{RHE}. Especially dark currents are more stable and closer to 0 A (Figure 40) for +0.39 V_{RHE}. Generally current differences are higher over a longer period of time when positive bias is applied. Independently of the chosen potential, samples with an additional window layer show increased stability of the current, with their degradation being delayed compared to the ones without window layers. The maximal achieved current density amounts only $j = -0.4\, mA/cm^2$, but still is at 75% of the initial value after 400 seconds. Compared to that, the bare glass/ITO/Cu_2O samples show a diminishing of the current to ~5% of the initial value after the same time duration.

Table 6 compares the current density measured at 0 V_{RHE} and +0.39 V_{RHE} bias over time. Although the initial current density is greater at 0 V_{RHE}, the rate of degradation is significantly higher than for +0.39 V_{RHE}.

Table 6: Current density of glass/ITO/Cu_2O/ZnOS/NTO at 0 V and +0.39 V vs. RHE

Applied potential (V_{RHE})	0	+0.39	0	+0.39
Time (s)	**Current difference (mA/cm^2)**		**Current difference (%)**	
0	-1	-0,4	100	100
100	-0,5	-0,4	50	100
200	-0,4	-0,35	40	87,5
300	-0,35	-0,3	35	75
400	-0,35	-0,3	35	75
500	-0,25	-0,25	25	62,5
600	/	-0,25	/	62,5
800	/	-0,25	/	62,5

/ no data available

For the photocathodes based on stainless steel, there is a similar trend noticeable in terms of current density and stability dependence on the applied potential (Figure 46). Analogous to glass/ITO substrates, the greatest current difference of up to $j = -2.35\ mA/cm^2$ was measured for 0 V_{RHE}, for the sample without window layers. The current density has decreased to ~17% of the initial value after only 400 seconds of illumination. The sample employing window layers (Figure 46) shows a significantly higher stability. Table 7 compares the absolute generated current densities (mA/cm^2) with their relative variation compared to the initial values (%) over time.

Table 7: Current differences of steel/Cu_2O/ZnOS/NTO at 0 V and +0.39 V vs. RHE

Applied potential (V_{RHE})	0	+0.39	0	+0.39
Time (s)	**Current difference (mA/cm^2)**		**Current difference (%)**	
0	-1,1	-0,2	100	100
200	-1,1	-0,3	100	150
400	-0,9	-0,3	81,8	150
600	-0,65	-0,3	59,1	150
800	-0,55	-0,25	50	125,0
1000	-0,45	-0,25	40,9	125,0
1200	/	-0,15	/	75,0
1400	/	-0,15	/	75,0

/ no data available

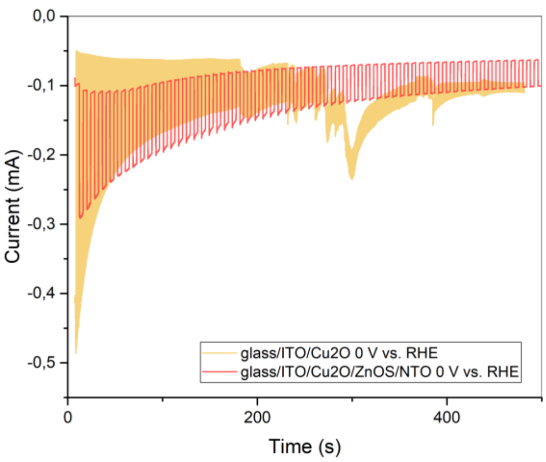

Figure 44: Stability test (chronoamperometry): Effect of ZnOS/NTO window layer on top of glass/ITO/Cu_2O at 0 V vs. RHE

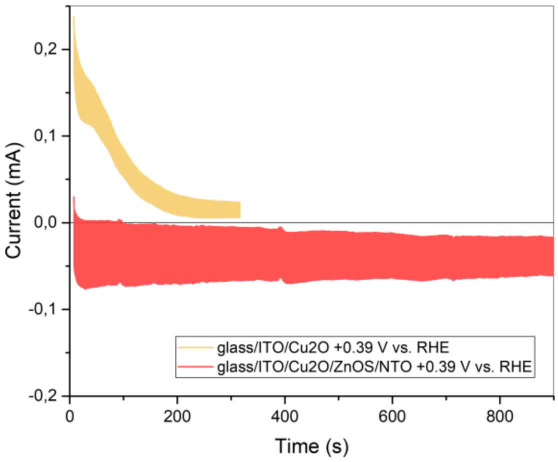

Figure 45: Stability test (chronoamperometry): Effect of ZnOS/NTO window layer on top of glass/ITO/Cu_2O at +0.39 V vs. RHE

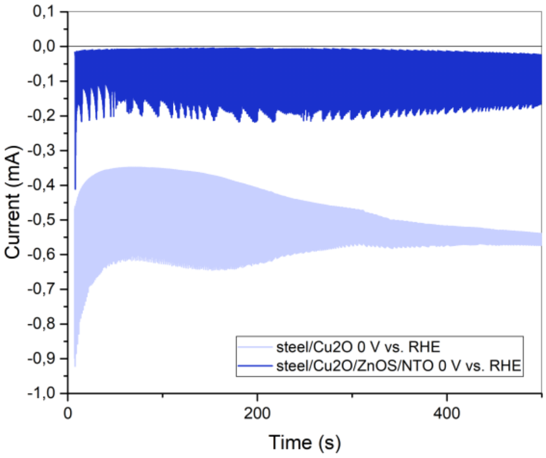

Figure 46: Stability test (chronoamperometry): Effect of ZnOS/NTO window layer on top of steel/Cu_2O at 0 V vs. RHE

5.1.2.3 **Effect of buffer layer – ZnO versus ZnOS**

Photocathodes with two buffer layers, ZnO and ZnOS were tested. The sample employing a ZnO buffer layer presented a lower dark current for a broader range of applied potential (Figure 47), which suggests a lower leakage current. However, the light current density is also smaller than the one of the sample employing the ZnOS buffer. Regarding the photocathodes' stabilities at 0 V_{RHE} (Figure 48), ZnO-employing photocathodes exhibit a sudden degradation, with the corresponding minimization of the photocurrent after ~300 sec, which is not observed for the ZnOS-employing photocathodes. Due to the higher stability of the ZnOS, most of the experiments were realized with this buffer layer.

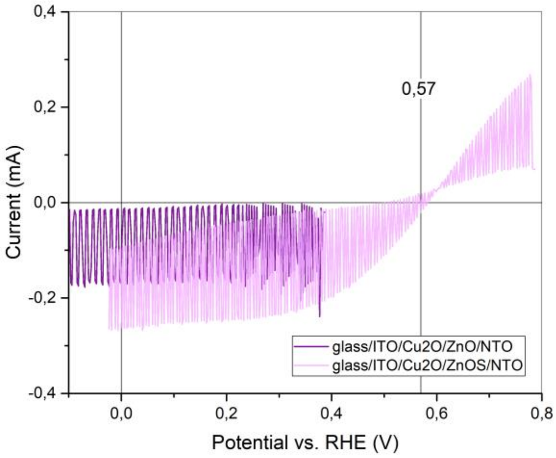

Figure 47: Linear sweep voltammogram: Effect of using ZnO or ZnOS as buffer layers on light and dark current at different potentials

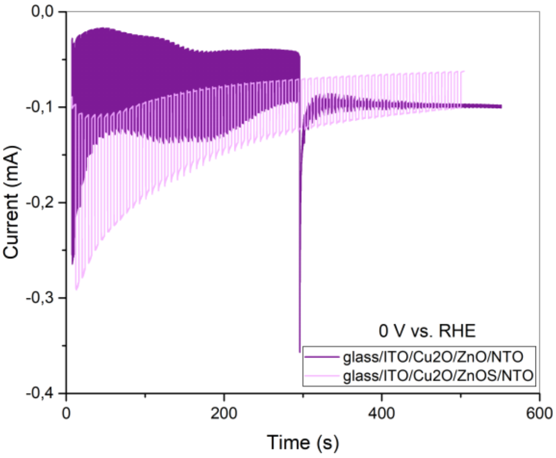

Figure 48: Stability test (chronoamperometry): Performance of ZnO and ZnOS buffer layers measured at 0 V vs. RHE

5.1.2.4 Effect of the electrolyte pH

For all the experiments conducted at pH=6 there was a clear difference of the obtained photocurrent and stability compared to the experiments conducted at pH=3 noticeable, with a significant decrease of the photocurrent and an increase in stability. The increased current densities achieved in acidic electrolyte could be due to an abundance of protons (H^+) and therefore higher probability of H^+ reduction to H_2, boosting HER. In addition, Pt-co-catalysts are reported to provide a H-binding energy 100 times higher in acidic than in alkaline environments. [92] On the other hand, degradation also contributes to the observed current, since it is likewise a process demanding charge carrier transfer (chapter 1.2).

H_2O's Pourbaix diagram (Figure 49) showcases at which potential and pH value, water, gaseous hydrogen and oxygen are stable. The two diagonal lines illustrate the system's equilibrium conditions, meaning that if the operating parameters lie below the bottom line (a), gaseous hydrogen will bubble off the electrode until equilibrium is reached. Respectively oxygen will form above the top line (b). Working in a more acidic environment therefore favors the hydrogen evolution reaction, especially when operating at lower bias. Applying reasonable potential is necessary for the reaction to be kinetically controlled. Nonetheless, with highly positive applied voltage, the occurring chemical reaction shifts towards the creation of H_2O from O_2 and H^+, which should be prohibited. At pH=6 and 0 V vs. RHE applied bias, stability of molecular water is favored whilst H^+ concentration diminishes. When increasing alkalinity even further, hydrogen evolution takes place directly by water reduction.

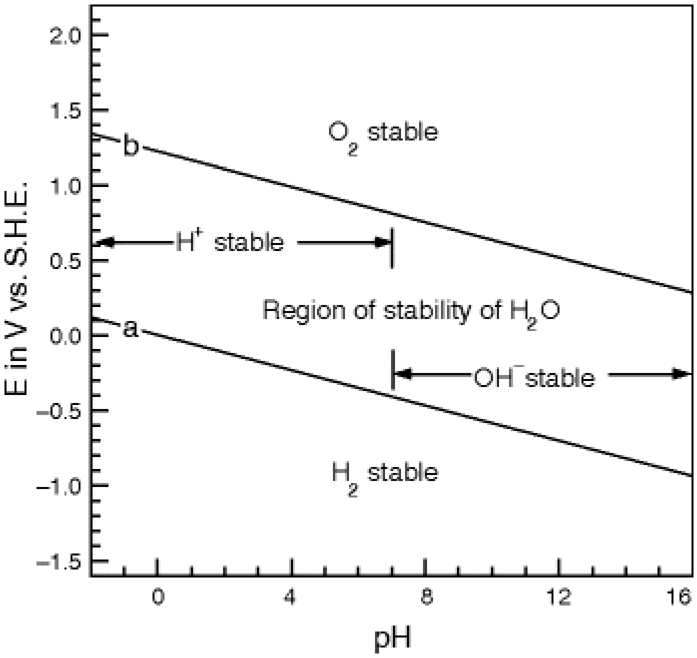

Figure 49: Pourbaix diagram of water [93]

For the bare Cu_2O photocathode stability tests (Figure 50), very little photocurrent has been created at pH=6. In return, stabilities can be slightly prolonged in a less acidic environment, due to lower H^+ concentration attacking the cell's surface, as well as general less current flow favoring the reduction process of the absorber material. Nonetheless, both working conditions cause quick degradation after less than 6 minutes. Similar behavior is noticeable with cells featuring a p-n junction (Figure 52). Although stability is significantly improved with both pH variations, a higher H^+ concentration results in greater current difference, despite dark current being substantially increased towards more negative values.

Also, slow reaction kinetics and current even in the positive regime at zero irradiation is eye-catching (Figure 52). For cells investigated at higher H^+ concentration, a steadier course of current is noticeable. Additionally, these cells provided with a window layer did not degrade at all, even after more than 8 minutes of irradiation.

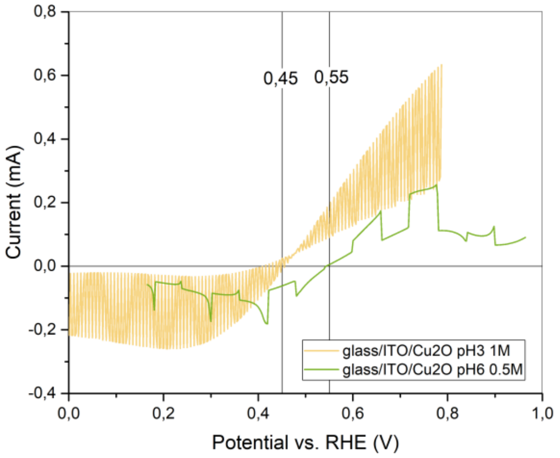

Figure 50: Linear sweep voltammogram: Effect of electrolyte's pH on unprotected glass/ITO/Cu₂O cells' onset potentials

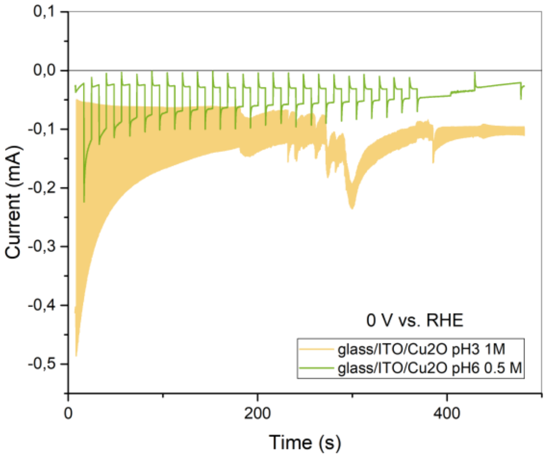

Figure 51: Stability test (chronoamperometry): Performance of bare glass/ITO/Cu₂O cells at pH=3 and pH=6 measured at 0 V vs. RHE

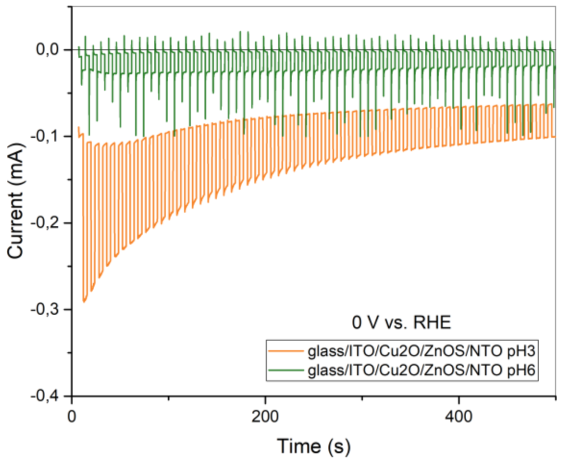

Figure 52: Stability test (chronoamperometry): Performance of window-layer-protected cells at pH=3 and pH=6 measured at 0 V vs. RHE

Figure 53 showcases, how investigating samples in acidic environment causes a yellow tint of the entire sample, but especially its radiation-exposed areas. Contrarily, at pH=6, spots mostly appear dark-grey to black. It has also been observed that generally samples investigated under large negative bias appear to develop deep black coloring, as well as greater tendency towards delamination (Figure 54). The reasons for this effect regarding eventually formed compounds are further investigated in 0. Another effect of exposing samples to increased voltage for large amount of time, is a change in the electrolyte's color from clear to yellow (Figure 55).

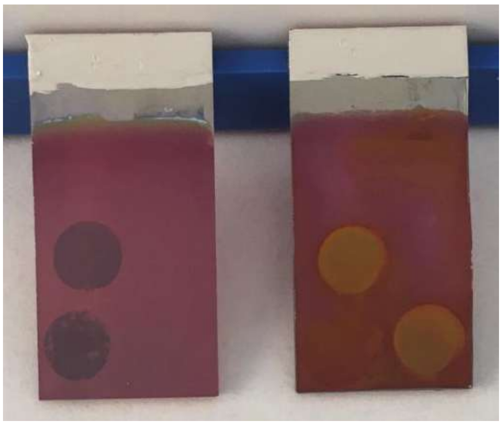

Figure 53: Differences in color of illuminated spots of glass/ITO/Cu2O/ZnOS/NTO samples measured at pH=6 (left) and pH=3 (right)

Figure 54: glass/ITO/Cu2O/ZnOS/NTO/Pt sample investigated at great bias of up to -1.2 V (LSV) and -0.9 V (stability test) versus Ag/AgCl

Figure 55: 0.5 M Na_2SO_4 electrolyte (pH=6) after measuring sample shown in Figure 53 at high anodic bias (right)

5.1.2.5 **Effect of Pt co-catalyst**

Adding a thin layer of co-catalyst (Pt, 3 nm) seems to increase the overall sample's stability even further compared to providing window layers only. The cells' onset potentials are not being influenced by this procedure, as shown in Figure 56. As for current creation, the deposition of Pt appears to result in a decrease of primarily light, but also dark current. A general issue with Platinum co-catalyst deposition is the diminishing efficiency due to shunting. Figure 57 illustrates the performance of a cell measured at 0 V_{RHE}, which shows fluctuations as well as overall decrease in current over time. In this case a resistance-less path appears to have formed for charge carriers to pass without creating any current. Nonetheless, in some cells fabricated under the same conditions, Platinum leads to increased current differences alongside enhanced stability (Figure 58).

Investigating the effect of depositing Platinum onto the entire sample's surface versus only within a certain, defined area using a so-called "mask", no clear conclusions could have been drawn and would need to be further investigated.

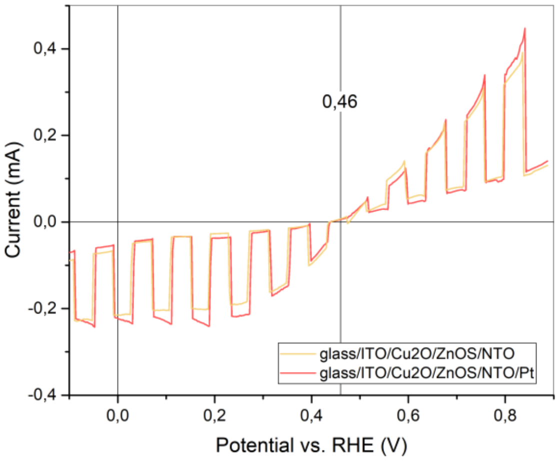

Figure 56: Linear sweep voltammogram: Effect of Platinum co-catalyst deposition on current creation under varying applied bias and onset potential

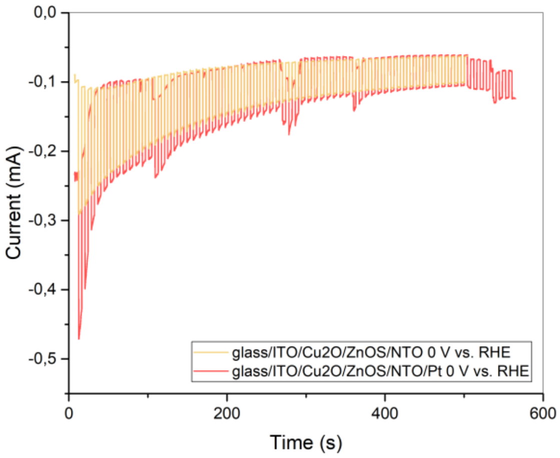

Figure 57: Stability test (chronoamperometry): Shunting of the cell equipped with a Pt co-catalyst layer of 3 nm

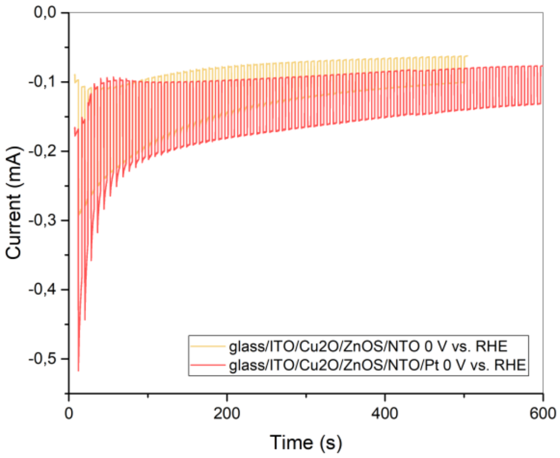

Figure 58: Stability test (chronoamperometry): Improved performance with adding a Pt co-catalyst layer of 3 nm

5.2 Scanning electron microscopy (SEM)

To be able to gain more insight about the degradation mechanisms of the photocathodes, these were characterized by SEM (plain view and cross section). The spot of the sample shown in Figure 59 (a)-(c) has not been measured (but immersed in the electrolyte of pH=3), whereas the spot in (d)-(f) has been measured at pH=3 and under illumination. There is a clear distinction visible between the two spots. Illuminated spots show severe degradation, especially when looking at the layer of cuprous oxide. Contrary to the non-illuminated areas, cavities extending to ~100 nm depth from the surface have formed. The window layers of ZnOS and especially NTO show less degradation, retaining their compactness over extended areas. However, the degradation of the Cu_2O from underneath, eventually leads to the collapse of the whole multilayer structure and oxidized particles were formed at the surface.

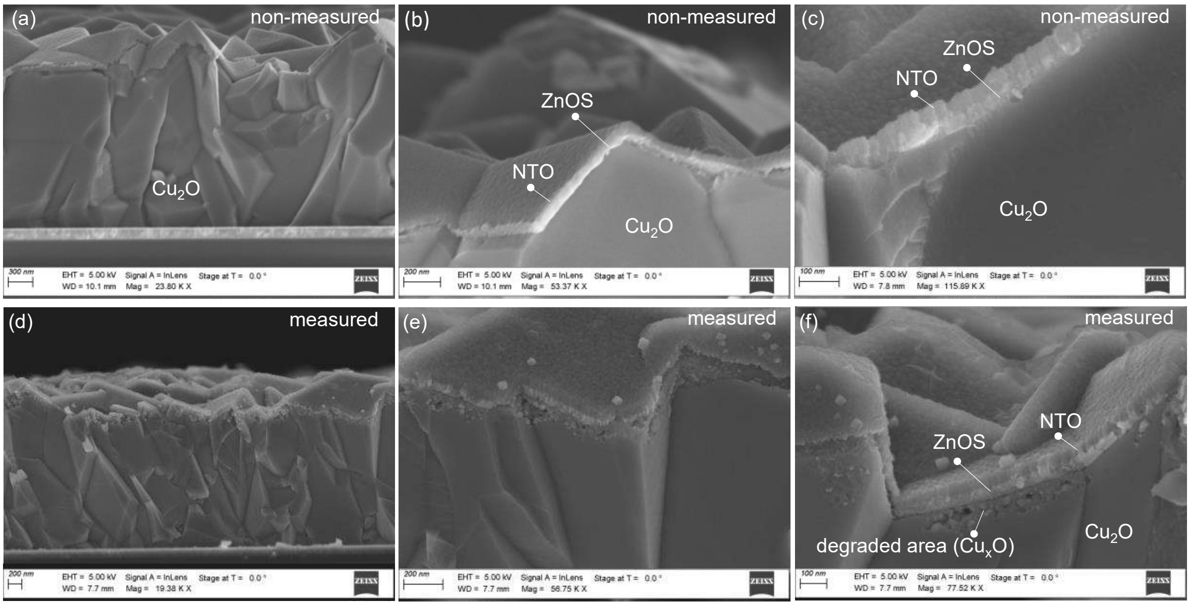

Figure 59: Cross-sectional SEM images of glass/ITO/Cu_2O/ZnOS/NTO after electrochemical testing. a) general view of all layers; b) closer view of less damaged sample spot; c), d) severely degraded sample areas

Comparing non-measured and measured samples containing a ZnO buffer layer (Figure 60), this degradation effect is even more noticeable. In images a)-c) compact alignment of the two window layers on top of the Cu_2O absorber is visible. However, after immersing the sample in 1M Na_2SO_4 solution at pH=3 and illuminating, severe degradation occurs primarily within the ZnO layer. Interestingly, the NTO passivation layer stays intact. Nonetheless, this does not appear to prevent the sample's performance to decrease in stability tests.

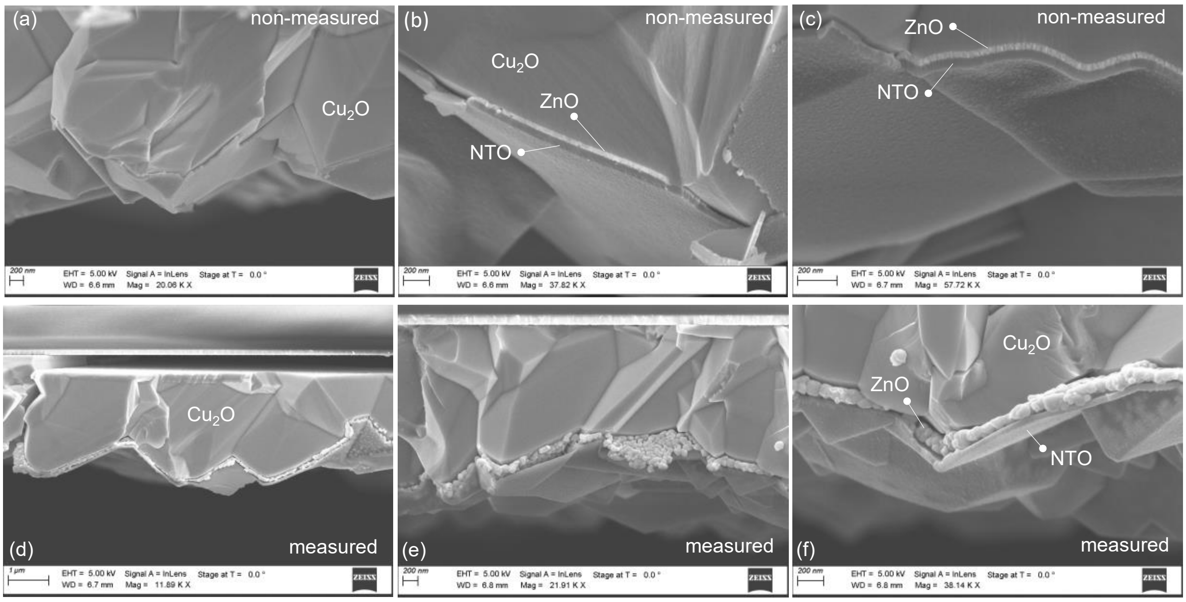

Figure 60: Cross-sectional SEM images of glass/ITO/Cu_2O/ZnO/NTO after electrochemical testing. a) general view of all layers of a non-measured spot; b), c) closer view of less damaged, non-measured sample spots; d), e), f) severely degraded sample areas after illumination and exposure to acidic environment

To explain this degradation, the hypothesis is that under illumination, in combination with exposure to the electrolyte, an oxidation process of Cu(I) occurs. Reaction XXIII describes the formation of cupric oxide from cuprous oxide. This could also explain the change in color of the illuminated spots, since CuO has higher absorption and a brown-ish colour. This hypothesis is further explored using XRD (5.3). Reaction XXIV would occur in further consequence.

$$Cu_2O \rightarrow CuO + Cu^{2+} + 2e^- \qquad XXIII$$

$$Cu^{2+} + 2e^- \rightarrow Cu \qquad XXIV$$

The sample shown in Figure 61 on steel substrate, was measured at pH=3. There is again a great difference in surface appearance when looking at illuminated and non-illuminated areas. With these top-view images, the formation of regularly spread clusters is even more apparent.

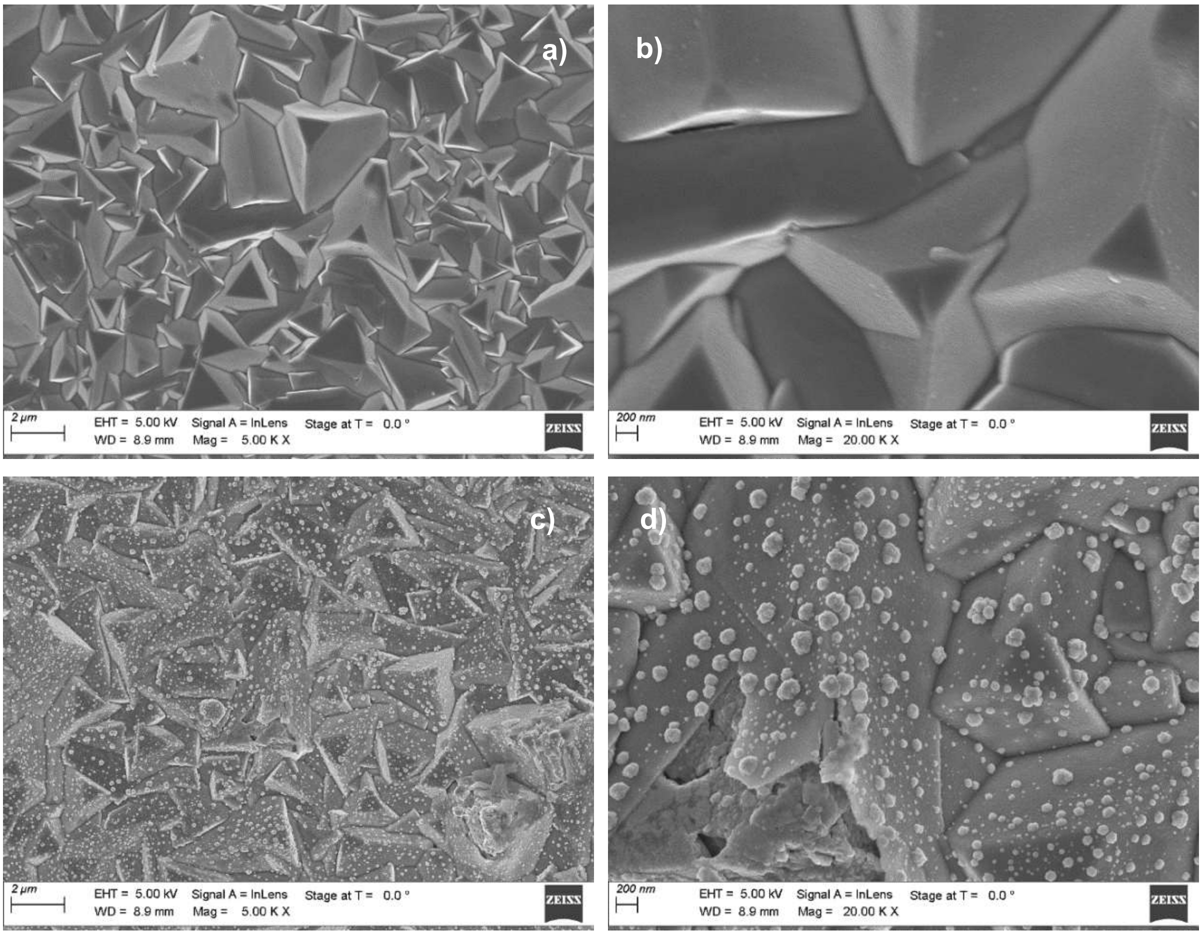

Figure 61: Top-view SEM image of measured steel/Cu_2O/ZnOS/NTO sample a) non-illuminated spot 5K magnification b) non-illuminated spot 20K magnification c) illuminated spot 5K magnification d) illuminated spot 20K magnification

5.3 X-ray diffractometry (XRD)

Further exploring the theory of CuO formation under illumination, samples were examined using XRD. Figure 62 compares: (a) a glass/ITO/Cu_2O photocathode at its unmeasured state (not yet immersed into the electrolyte solution), with (b) a spot on the photocathode that was immersed in the electrolyte but not illuminated and (c) a spot that was immersed and illuminated at -0.39 V vs. RHE. All diffractograms were recorded at an X-ray incidence angle of $\omega = 2°$ and show their main peak at $2\theta = 37°$, which corresponds to the [111] Cu_2O reflection according to the reference cuprite spectrum. All other peaks for cases (a) and (b) can be ascribed to the cuprite crystal structure, although some minor reflections of the tenorite (CuO) are in close proximity to the one of cuprite. This means that we cannot exclude traces of CuO.

However, for the illuminated spot, additional peaks at $2\theta = 39.7°, 46.4°$ and $67.0°$ appear, which can be identified with tenorite's [111], eventually [20-2] and [220] reflection peaks. It is therefore concluded that the electrochemical measurement of the photocathode under illumination led to the oxidation of the absorber.

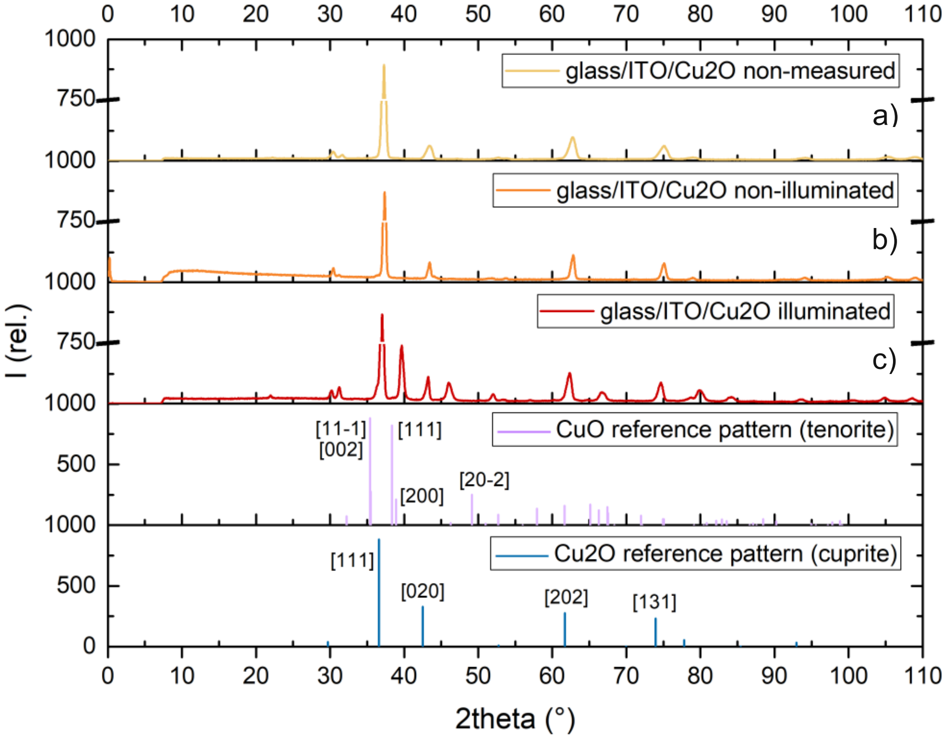

Figure 62: XRD spectra of non-measured (a), non-illuminated (b) and illuminated (c) glass/ITO/Cu_2O sample areas executed at ω=2°, as well as CuO and Cu_2O reference patterns

For the photocathodes of glass/ITO/Cu_2O/ZnOS/NTO, the X-Ray diffractograms for the non-illuminated and illuminated spots measured under a bias of 0 V vs. RHE at an angle of ω=2° are very similar and consistent with the reflection peaks of cuprite. Only if the X-Ray angle of incidence is decreased to ω=0.5° (more pronounced grazing incidence) does the diffractogram of the illuminated spot differentiate, showing peaks that can be ascribed to tenorite (CuO). This suggests that the degradation of the Cu_2O absorber is maybe delayed through the employment of window layers, but it is nevertheless taking place eventually.

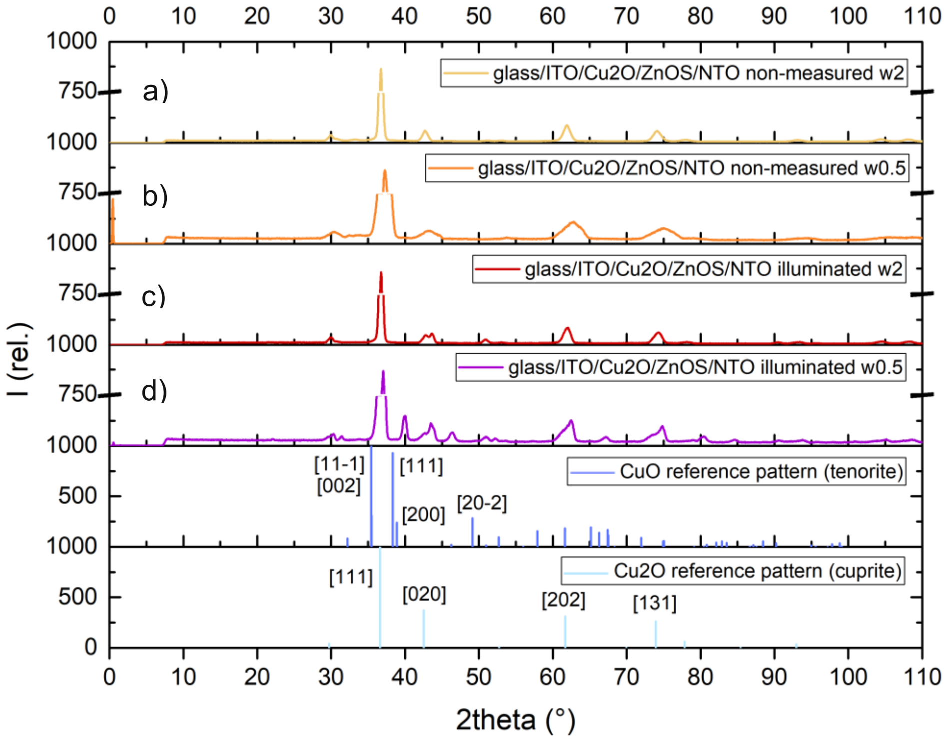

Figure 63: Non-measured a), b) versus electrolyte immersed and illuminated c), d) glass/ITO/Cu_2O/ZnOS/NTO photocathodes at ω=2° versus ω=0.5° measuring angle

6. Summary

Photocathodes based on glass/ITO or steel foil substrates with an absorber layer made from cuprous oxide were successfully synthesized. The electrochemical deposition of Cu_2O on glass/ITO was improved by introducing a dual-potential process to optimize the nucleation as well as growth process for a more homogenous thin film. X-ray diffractograms confirmed the deposition of pure cuprous oxide.

With bare electrodeposited Cu_2O absorber layers, current differences of $j = -2.15\,mA/cm^2$ (glass/ITO) to $j = -2.35\,mA/cm^2$ (steel) were achieved. These values theoretically equal a solar-to-hydrogen efficiency of 2.6% and 2.9% respectively at a sample area of 0.2 cm^2. Nonetheless, it is important to note, that experimentally derived current differences of light and dark current are not necessarily solely due to photon absorption and in further consequence charge separation within the p-n junction. Other processes, such as degradation caused by self-redox reactions, which are very common for cuprite, can influence light current and therefore the resulting current differences.

Regarding the photocathode's stability, the addition of a ZnOS buffer and NTO passivation layer improved the overall performance, causing current to sustain for up to 2000 seconds, whilst bare substrate/Cu_2O cathodes significantly degraded after 200 seconds.

Additionally, by creating a p-n junction through providing a window layer, glass/ITO-based samples' onset potentials increased. Contrarily, for steel-based cathodes, the creation of a p-n junction did not influence their onset potential, showcasing that this effect is dependent on individual material properties. Maximal current differences with Cu_2O/ZnOS/NTO samples however amounted $j = -1\,mA/cm^2$ (glass/ITO) to $j = -1.1\,mA/cm^2$ (steel).

The best working environment for majority of the samples appeared to be an acidic 1 M Na_2SO_4 solution of pH=3, with no additional stirring, alongside external applied bias of $< 0.4\ V_{RHE}$ (mostly $0\ V_{RHE}$) under front illumination.

Concerning the structural effects of measuring photocathodes in said environment, degradation of Cu_2O was a major issue. As shown in SEM images, even though decomposition of cuprous oxide was prolonged after the addition of window layers, non-bulk absorber material still was damaged, whilst the window layers – specially NTO – appeared to stay intact. Nonetheless, with more and more absorber material degrading, the overall structure collapsed at some point, resulting in a significant loss of the cell's performance.

When comparing non-measured with illuminated samples by XRD analysis, there is a clear shift of the entire Cu_2O spectrum towards higher angles noticeable. This indicates lattice deformation under loss of crystal volume; most probably Cu atoms. Furthermore, with additional peaks showing at certain characteristic angles, the formation of CuO is very likely.

7. Outlook

7.1 pH value

Since there were clear differences in a PEC cell's performance depending on its working environment, the pH value is a topic worth further exploring. It appears to be a balancing act between good photocurrent and prevention of degradation with acidic (pH=3) and more neutral (pH=6) electrolytes respectively. As proposed by literature, a membrane separating an acidic, HER promoting solution from an alkaline, OER promoting one, could be a way to combat this issue. [92] In this case, the cathode would be placed in a solution of high H^+ concentration to promote reduction, whereas the anode is surrounded by mainly OH^- ions for the oxidation reaction. Furthermore, separating the electrolyte by an ion-selective membrane allows to maintain the pH in each cell compartment. A setup providing a gas-separating membrane would additionally prevent developed O_2 and H_2 from reacting, which would mean loss in hydrogen gas for fuel, as well as being endangering since it's a matter of an explosive combustion.

7.2 Co-catalyst

Experimental data from this study have not shown any improvement of HER by utilizing a platinum co-catalyst, despite this effect being commonly reported in literature. In fact, depositing an additional Pt layer did not make any difference or even worsened the cell's overall performance – independently of using a shadow mask or not. By optimizing co-catalyst deposition, as well as this material's working environment, the rate of photocatalytic reactions should be enhanced by providing active sites, as well as boosting photogenerated charge separation. Since the water splitting reaction consist of two half reactions, an optimized PEC cell calls for two different types of catalyst. As proposed by literature, a dual-co-catalyst would ensure both, the proton reduction, as well as water oxidation, are supported. Especially the OER reaction appears to be challenging to accelerate, since water oxidation requires a multistep process demanding greater activation energy to proceed. It has been shown, that providing a dual-co-catalyst could even result in much higher activities than the sum of the two individual catalysts. [37] Apart from the material itself, proper alignment on the semiconductor surface might also be a contributing factor for boosting the water splitting reaction. In order to transfer the photogenerated e^- and h^+ as quickly as possible to enable reduction and respectively oxidation reactions before recombination takes place, it is helpful to consider the co-catalysts' locations. This means placing the reduction co-catalyst (usually noble metals, such as Pt, Pd, Rh, Au) on the electron-demanding and the oxidation one (usually metal oxides, such as RuO_2, IrO_2) on the hole-demanding site. [37]

7.3 Band engineering

Another possibility of optimizing a PEC cell, is by band-gap engineering. This process describes alteration of a material's band gap through exemplarily doping, creating alloys, or layering certain semiconductors so their individual band gaps influence each other in a supportive manner. Narrowing band gaps would allow a broader range of the solar spectrum to be used to excite electrons from the valence band. Nevertheless, a band gap of at least 1.6 eV is necessary to perform the water splitting reaction. Instead of only operating within the UV-vis spectrum, even absorption within the near IR region is possible. [37] Consequently, enabling absorption of lower frequency photons entails utilizing more of the sun's energy and therefore harvesting more solar light.

7.4 Resistance

Despite going the route of improving a cell's desired properties, there is also the need of preventing unwanted reactions. There are many causes of loss in efficiency, which even the theoretically most efficient absorber cannot compensate for. Concerning issues with charge transfer processes, series resistance and shunt resistance are significantly limiting factors, which correlate with fabrication quality. To prevent shunt resistance, the avoidance of electrolyte intercalating into pinholes is evident. Therefore, optimization of the fabrication process itself or eventual follow-up treatment are topics to further investigate. Series resistance is a matter of electrolyte transport through solution (= solution resistance), implying the necessity of continuing studying the electrolyte's composition, concentration, and temperature. Series resistance also includes interfacial resistance at different materials' layers' interfaces (especially semiconductor/catalyst interfaces), which is a question of material choice as well as, again, fabrication method. [94, 95]

8. Conclusion

In the end, there are still numerous issues and uncertainties to be further addressed. The main reasons for loss in PEC cell efficiency are recombination processes of photo-excited e^-/h^+ pairs, resistance within electrodes or electrical connections, as well as voltage losses at the contacts. Furthermore, many aspects of the bond breaking and forming in the water splitting reaction, as well as individual material's influences on each other (*e.g.* band bending) are still needed to be understood. Finding optimal fabrication, as well as working conditions also is a major matter to be explored. Altogether, by fully understanding occurring processes along with tailoring specific materials' effects to them, it is strongly believed to find a way of creating robust, environmentally friendly, low-cost and scalable photoelectrochemical cells with great efficiency to perform water splitting.

9. Abbreviations

A

AM	*air mass*
APCE	*absorbed-incident-photon-to-current conversion efficiency*

B

BV	*Butler-Volmer*

C

CA	*chronoamperometry*
CBM	*conduction band minimum*
CE	*counter electrode*

D

DC	*direct current*

E

ECD	*electrochemical deposition*
EDX	*energy-dispersive X-ray spectroscopy*

F

FTO	*fluorine-doped tin oxide*

G

GHG	greenhouse gas

H

HER	*hydrogen evolution reaction*
HV	*high vacuum*

I

IPCE	*incident-photon-to-current conversion efficiency*
ITO	*indium-tin-oxide*

L

LSV	*linear sweep voltammetry*

N

NHE	*normal hydrogen electrode*
NTO	*niobium-doped titanium oxide*

O

OER	*oxygen evolution reaction*
ORR	*oxygen reduction reaction*

P

PEC	*photoelectrochemical*
PV	*photovoltaic*
PVE	*photovoltaic-electrolysis*

R

RE	*reference electrode*
RF	*radio frequency*
RHE	*reversed hydrogen electrode*

S

SEM	*scanning electron microscopy*
S-H	*Scharifker-Hills*
STH	*solar-to-hydrogen*

T

TCO	*transparent conducting oxide*

U

UV-vis	*ultraviolett-visible*

V

VB	*valence band*
VBM	*valence band maximum*

W

WE	*working electrode*

X

XRD	*X-ray diffractometry*

10. References

1. Pappas, S. *Carbon Dioxide Is Warming the Planet*. 2017 [cited 2021 03.01.]; Available from: https://www.livescience.com/58203-how-carbon-dioxide-is-warming-earth.html.
2. *Global Climate Change: Vital Signs of the Planet*. The Causes of Climate Change 2020 [cited 2021 03.01.]; Available from: https://climate.nasa.gov/causes/.
3. Osterloh, F.E., *Inorganic nanostructures for photoelectrochemical and photocatalytic water splitting.* Chemical Society Reviews, 2012.
4. Edenhofer, O., R. Pichs-Madruga, Y. Sokona, E. Farahani, S. Kadner, K. Seyboth, A. Adler, I. Baum, S. Brunner, P. Eickemeier, B. Kriemann, J. Savolainen, S. Schlömer, C. von Stechow, T. Zwickel, J.C. Minx *AR5 Climate Change 2014: Mitigation of Climate Change*. 2014, Intergovernmental Panel on Climate Change (IPCC): Cambridge, United Kingdom and New York, NY, USA.
5. Sönnichsen, N. *Primary energy - global consumption 2000-2019*. 2020.
6. Ritchie, H. *Electricity Mix*. Our World in Data 2020 [cited 2021 19.05.]; Available from: https://ourworldindata.org/electricity-mix?country=.
7. Agency, I.E., *World Energy Outlook 2020*, O. 2020, Editor. 2020.
8. Green, M.A., et al., *Solar cell efficiency tables (Version 55).* Progress in Photovoltaics: Research and Applications, 2020. **28**(1): p. 3-15.
9. Green, M., et al., *Solar cell efficiency tables (version 57).* Progress in Photovoltaics: Research and Applications, 2021. **29**(1): p. 3-15.
10. *Lazard's Levelized Cost of Energy Analysis—Version 14.0.* Lazard: New York, NY, USA, 2020: p. 21.
11. Pedro Migowski, A.F.F., *Uses of Physical Vapor Deposition Processes in Photoelectrochemical Water Splitting Systems.* Recyclable Catalysts, 2016. **3**: p. 1-12.
12. *Green Hydrogen Supply: A Guide to Policy Making*. 2021, IRENA International Renewable Energy Agency.
13. Grimm, A., W.A. de Jong, and G.J. Kramer, *Renewable hydrogen production: A techno-economic comparison of photoelectrochemical cells and photovoltaic-electrolysis.* International Journal of Hydrogen Energy, 2020. **45**(43): p. 22545-22555.
14. Sun, X., et al., *Earth-abundant electrocatalysts in proton exchange membrane electrolyzers.* Catalysts, 2018. **8**(12): p. 657.
15. Acar, C., *Solar Hydrogen's Role for a Sustainable Future*, in *Accelerating the Transition to a 100% Renewable Energy Era*, T.S. Uyar, Editor. 2020, Springer International Publishing: Cham. p. 309-331.
16. Ramazan Asmatulu, W.S.K., *Chapter 8 - Electrospun nanofibers for catalyst applications*, in *Synthesis and Applications of Electrospun Nanofibers - A volume in Micro and Nano Technologies*. 2019, Elsevier. p. 306.
17. Wick, R. and S.D. Tilley, *Photovoltaic and Photoelectrochemical Solar Energy Conversion with Cu2O.* The Journal of Physical Chemistry C, 2015. **119**(47): p. 26243-26257.
18. Michael G. Walter, E.L.W., James R. McKone, Shannon W. Boettcher†, Qixi Mi, Elizabeth A. Santori, and Nathan S. Lewis, *Solar Water Splitting Cells.* Chemical Reviews, 2010. **110**(11): p. 6446–6473.
19. Hariprasad Narayananab, B.V., Konda Ramasamy Krishnamurthya, Harindranathan Nair, *Chapter 12 - Hydrogen from photo-electrocatalytic water splitting*, in *Solar Hydrogen Production - Processes, Systems and Technologies*, M.D.D.A. Francesco Calise, Massimo Santarelli, Andrea Lanzini, Domenico Ferrero, Editor. 2019, Academic Press: India. p. 419-486.
20. Hisatomi, T., K. Takanabe, and K. Domen, *Photocatalytic Water-Splitting Reaction from Catalytic and Kinetic Perspectives.* Catalysis Letters, 2015. **145**(1): p. 95-108.
21. Reichert, R., Z. Jusys, and R.J. Behm, *Au/TiO2 Photo(electro)catalysis: The Role of the Au Cocatalyst in Photoelectrochemical Water Splitting and Photocatalytic H2 Evolution.* The Journal of Physical Chemistry C, 2015. **119**(44): p. 24750-24759.

22. Fu, S.C., et al., *Bio-inspired cooling technologies and the applications in buildings.* Energy and Buildings, 2020. **225**: p. 110313.
23. *Chapter 13 - Advanced and Low Cost Energy and Lighting Devices*, in *Fundamentals and Applications of Nano Silicon in Plasmonics and Fullerines*, M. Nayfeh, Editor. 2018, Elsevier. p. 363-429.
24. Jiang, C., et al., *Photoelectrochemical devices for solar water splitting–materials and challenges.* Chemical Society Reviews, 2017. **46**(15): p. 4645-4660.
25. Tawfik, W.Z., et al., *Highly conversion efficiency of solar water splitting over p-Cu2O/ZnO photocatalyst grown on a metallic substrate.* Journal of Catalysis, 2019. **374**: p. 276-283.
26. Beata Bajorowicz, M.P.K., Anna Malankowska, Paweł Mazierski, Joanna Nadolna, Aleksandra Pieczyńska, Adriana Zaleska-Medynska, *Application of metal oxide-based photocatalysis*, in *Metal Oxide-Based Photocatalysis*. 2018, Elsevier. p. 211-340.
27. Shiyou Chen, L.-W.W., *Thermodynamic Oxidation and Reduction Potentials of Photocatalytic Semiconductors in Aqueous Solution.* Chemistry of Materials, 2012. **24**(18): p. 3659-3666.
28. Hemmerling, J.R., A. Mathur, and S. Linic, *Design Principles for Efficient and Stable Water Splitting Photoelectrocatalysts.* Accounts of Chemical Research, 2021. **54**(8): p. 1992-2002.
29. W. Zhao, Y.J., C.H. Gao, W. Gu, Z.M. Jin, Y.L. Lei, L.S. Liao, *A simple method for fabricating pen junction photocatalystCuFe2O4/Bi4Ti3O12and its photocatalytic activity.* Materials Chemistry and Physics, 2014. **143**(3): p. 952-962.
30. Ryan P. Smith, A.A.-C.H., Tobias Beetz, Erik Helgren, *Introduction to semiconductor processing: Fabrication and characterization of p-n junction silicon solar cells.* American Journal of Physics, 2018. **86**(740).
31. *Electronics Tutorials*. PN Junction Theory [cited 2021 24.05.]; Available from: https://www.electronics-tutorials.ws/diode/diode_2.html.
32. Paracchino, A., et al., *Highly active oxide photocathode for photoelectrochemical water reduction.* Nat Mater, 2011. **10**(6): p. 456-61.
33. Wei Hu, J.Y., *Two-dimensional van der Waals heterojunctions for functional materials and devices.* Journal of Materials Chemistry C, 2017. **5**(47): p. 12289-12297.
34. Föll, H. *5.3.1 Ideal Heterojunctions*. [cited 2021 25.05.]; Available from: https://www.tf.uni-kiel.de/matwis/amat/semi_en/kap_5/backbone/r5_3_1.html.
35. Dasgupta, U., A. Bera, and A.J. Pal, *Band Diagram of Heterojunction Solar Cells through Scanning Tunneling Spectroscopy.* ACS Energy Letters, 2017. **2**(3): p. 582-591.
36. Sebastian Siol, J.C.H., S. David Tilley, Michael Graetzel, Jan Morasch, Jonas Deuermeier, Wolfram Jaegermann, Andreas Klein, *Band Alignment Engineering at Cu2O/ZnO Heterointerfaces.* ACS Applied Materials & Interfaces, 2016. **8**(33): p. 21824-21831.
37. Li, R. and C. Li, *Chapter One - Photocatalytic Water Splitting on Semiconductor-Based Photocatalysts*, in *Advances in Catalysis*, C. Song, Editor. 2017, Academic Press. p. 1-57.
38. Pan, L., et al., *Cu2O photocathodes with band-tail states assisted hole transport for standalone solar water splitting.* Nature Communications, 2020. **11**(1): p. 318.
39. Shi, X., et al., *General Characterization Methods for Photoelectrochemical Cells for Solar Water Splitting.* ChemSusChem, 2015. **8**(19): p. 3192-3203.
40. Li, C., et al., *Positive onset potential and stability of Cu2O-based photocathodes in water splitting by atomic layer deposition of a Ga2O3 buffer layer.* Energy & Environmental Science, 2015. **8**(5): p. 1493-1500.
41. Moehl, T., et al., *Investigation of (leaky) ALD TiO2 protection layers for water-splitting photoelectrodes.* ACS applied materials & interfaces, 2017. **9**(50): p. 43614-43622.
42. Bak, T., et al., *Photo-electrochemical hydrogen generation from water using solar energy. Materials-related aspects.* International Journal of Hydrogen Energy, 2002. **27**(10): p. 991-1022.
43. Mazzi, A., *Modeling and production of metal nanoparticles through laser ablation and applications to photocatalytic water oxidation*. 2017.
44. Mayer, M.T., *Photovoltage at semiconductor–electrolyte junctions.* Current Opinion in Electrochemistry, 2017. **2**(1): p. 104-110.

45. Lewerenz, H.J. and I.D. Sharp, *Chapter 1 Concepts of Photoelectrochemical Energy Conversion and Fuel Generation*, in *Integrated Solar Fuel Generators*. 2019, The Royal Society of Chemistry. p. 1-42.
46. Huan Qi, J.W., Denis Fichou, Zhong Chen, *Cu2O Photocathode for Low Bias Photoelectrochemical Water Splitting Enabled by NiFe-Layered Double Hydroxide Co-Catalyst.* Nature Scientific Reports, 2016. **6**(30882).
47. Dipika Sharma, S.U., Vibha R. Satsangi, Rohit Shrivastav, Umesh V. Waghmare, Sahab Dass, *Improved Photoelectrochemical Water Splitting Performance of Cu2O/SrTiO3 Heterojunction Photoelectrode.* Journal of Physical Chemistry C, 2014. **118**(44): p. 25320-25329.
48. Soolmaz Jamali, A.M., *Improving photo-stability and charge transport properties of Cu2O/CuO for photo-electrochemical water splitting using alternate layers of WO3or CuWO4produced by the same route.* Applied Surface Science, 2017. **419**: p. 269-276.
49. Wang, Y.C., et al., *Cu2O photocathodes for unassisted solar water-splitting devices enabled by noble-metal cocatalysts simultaneously as hydrogen evolution catalysts and protection layers.* Nanotechnology, 2019. **30**(49): p. 495407.
50. Tuo Wang, Y.W., Xiaoxia Chang, Chengcheng Li, Ang Li, Shanshan Liu, Jijie Zhang, Jinlong Gong, *Homogeneous Cu2O p-n junction photocathodes for solar water splitting.* Applied Catalysis B: Environmental, 2018. **226**: p. 31-37.
51. Chia-Yu Lin, Y.-H.L., Dirk Mersch, Erwin Reisner, *Cu2O|NiOx nanocomposite as an inexpensive photocathode in photoelectrochemical water splitting.* Chemical Science, 2012. **3**(12): p. 3482-3487.
52. Pan, L., et al., *Boosting the performance of Cu2O photocathodes for unassisted solar water splitting devices.* Nature Catalysis, 2018. **1**(6): p. 412-420.
53. Zhou, Y., et al., *Direct correlation between work function of indium-tin-oxide electrodes and solar cell performance influenced by ultraviolet irradiation and air exposure.* Physical Chemistry Chemical Physics, 2012. **14**(34): p. 12014-12021.
54. *Sustainability*. [cited 2021 04.06.]; Available from: https://www.worldstainless.org/sustainability/.
55. Ludlum, A., *Stainless Steels Chromium-Nickel Types 302 (S30200), 304 (S30400), 304L (S30403), 305 (S30500).* TECHNICAL DATA BLUE SHEET, 2004.
56. Helmenstine, A.M., Ph.D. *ThoughtCo*. Table of Electrical Resistivity and Conductivity 2019 [cited 2021 03.06.]; Available from: https://www.thoughtco.com/table-of-electrical-resistivity-conductivity-608499.
57. Golden, T.D., et al., *Electrochemical Deposition of Copper(I) Oxide Films.* Chemistry of Materials, 1996. **8**(10): p. 2499-2504.
58. *Copper(I) Oxide*. [cited 2021 30.05.]; Available from: https://www.americanelements.com/copper-i-oxide-1317-39-1.
59. Matias Ezequiel Aguirre, et al., *Cu2O/TiO2 heterostructures for CO2 reduction through a direct Z-scheme: Protecting Cu2O from photocorrosion.* Applied Catalysis B: Environmental 2017. **217**(15): p. 485-493.
60. Kunturu, P.P. and J. Huskens, *Efficient Solar Water Splitting Photocathodes Comprising a Copper Oxide Heterostructure Protected by a Thin Carbon Layer.* ACS Applied Energy Materials, 2019. **2**(11): p. 7850-7860.
61. Sawicka-Chudy, P., et al. *Numerical analysis and optimization of Cu2O/TiO2, CuO/TiO2, heterojunction solar cells using SCAPS.* in *Journal of Physics: Conference Series*. 2018. IOP Publishing.
62. Minami, T., Y. Nishi, and T. Miyata, *Efficiency enhancement using a Zn1− x Ge x-O thin film as an n-type window layer in Cu2O-based heterojunction solar cells.* Applied Physics Express, 2016. **9**(5): p. 052301.
63. Pan, J., C. Yang, and Y. Gao, *Investigations of cuprous oxide and cupric oxide thin films by controlling the deposition atmosphere in the reactive sputtering method.* Sens. Mater, 2016. **28**(7): p. 817-824.
64. Markus Soldemo, J.H.S., Zahra Besharat, Milad Ghadami Yazdi, Anneli Önsten, Christofer Leygraf, Mats Göthelid, Tore Brinck, Jonas Weissenrieder, *The Surface Structure of Cu2O(100).* The Journal of Physical Chemistry C, 2016. **120**(8): p. 4373–4381.

65. de Jongh, P.E., D. Vanmaekelbergh, and J.J. Kelly, *Cu2O: Electrodeposition and Characterization.* Chemistry of Materials, 1999. **11**(12): p. 3512-3517.
66. Wong, T.K., et al., *Current status and future prospects of copper oxide heterojunction solar cells.* Materials, 2016. **9**(4): p. 271.
67. Niu, W., et al., *Photoresponse enhancement of Cu2O solar cell with sulfur-doped ZnO buffer layer to mediate the interfacial band alignment.* Solar Energy Materials and Solar Cells, 2016. **144**: p. 717-723.
68. Meyer, B.K., et al., *Structural properties and bandgap bowing of ZnO1−xSx thin films deposited by reactive sputtering.* Applied Physics Letters, 2004. **85**(21): p. 4929-4931.
69. Yu, S.Y., et al., *Optical and Structural Analysis of Zinc Oxysulfide Digital Alloys Grown by Atomic Layer Deposition.* Journal- Korean Physical Society, 2018. **73**: p. 649-655.
70. Polity, A., et al., *ZnO based ternary transparent conductors.* Physica Status Solidi (a), 2006. **203**: p. 2867-2872.
71. Campbell, S.A., et al., *Titanium Dioxide (TiO2)-Based Gate Insulators.* IBM Journal of Research and Development, 1999. **43**: p. 383-392.
72. Balagurov, L., et al., *Electrical conductivity of titanium dioxide layers doped with vanadium, cobalt, and niobium.* Russian Microelectronics, 2012. **41**.
73. *Mathematica ElementData*. Technical data for Platinum [cited 2021 10.06.]; Available from: https://periodictable.com/Elements/078/data.html.
74. Chen, T., et al., *Identification of Copper(II)–Lactate Complexes in Cu2O Electrodeposition Baths: Deprotonation of the α-Hydroxyl Group in Highly Concentrated Alkaline Solution.* Journal of The Electrochemical Society, 2018. **165**: p. D444-D451.
75. Mohra, D., et al., *The investigation of electrodeposited Cu2O/ITO layers by chronocoulometry process: Effect of electrical potential.* Chinese Journal of Semiconductors IOP, 2016. **37**.
76. Laidoudi, S., et al., *Growth and characterization of electrodeposited Cu2O thin films.* Semiconductor Science and Technology, 2013. **28**.
77. Schennach, A.U.-P.D.M.R., *Electrochemical Kinetics of Corrosion and Passivity*. Graz University of Technology Institute of Solid State Physics: Graz, Austria.
78. Pala, D.R.G.S. *Activation Overpotential*. [cited 2021 01.07.]; Available from: http://home.iitk.ac.in/~vidtan/ElectrochemistryNotes/ActivationOverpotential_290615.pdf.
79. Kaur, J., et al., *All-oxide solar cells based on electrodeposited Cu2O absorber and atomic layer deposited ZnMgO on precious-metal-free electrode.* Solar Energy Materials and Solar Cells, 2017. **161**: p. 449-459.
80. Mazaira, D., et al., *The development of theoretical models for multiple nucleation with diffusion-controlled three-dimensional growth*. 2008. p. 1-24.
81. Wang, F., H. Xiao, and H. He, *Effects of applied potential and the initial gap between electrodes on localized electrochemical deposition of micrometer copper columns.* Scientific Reports, 2016. **6**(1): p. 26270.
82. Allnatt, A.R. and P.W.M. Jacobs, *Theory of nucleation in solid state reactions.* Canadian Journal of Chemistry, 1968. **46**(2): p. 111-116.
83. Scharifker, B. and G. Hills, *Theoretical and experimental studies of multiple nucleation.* Electrochimica Acta, 1983. **28**: p. 879-889.
84. Isaev, V.A., O.V. Grishenkova, and Y.P. Zaykov, *On the theory of 3D multiple nucleation with kinetic controlled growth.* Journal of Electroanalytical Chemistry, 2018. **818**: p. 265-269.
85. Guo, L., et al., *Island growth in electrodeposition.* Journal of Physics D: Applied Physics, 2011. **44**: p. 443001.
86. Hyde, M.E., *Scanning probe microscopy and electrochemical studies of deposition on electrode surfaces*. 2005, University of Oxford.
87. Shang, Y. and L. Guo, *Facet-Controlled Synthetic Strategy of Cu2O-Based Crystals for Catalysis and Sensing.* Advanced Science, 2015. **46**.
88. Joseph, S. and P.V. Kamath, *Electrochemical deposition of Cu2O on stainless steel substrates: Promotion and suppression of oriented crystallization.* Solid State Sciences, 2008. **10**(9): p. 1215-1221.
89. MOLE, M. *Pourbaix diagram*. Advanced Electrochemistry [cited 2021 08.07.]; Available from: https://monomole.com/advanced-electrochemistry-10/.

90. Inc., A.E. *Magnetron sputtering*. [cited 2021 10.07.]; Available from: https://angstromengineering.com/.
91. Hughes, M. *What is RF Sputtering?* News & Articles 2016 [cited 2021 10.07.]; Available from: http://www.semicore.com/news/92-what-is-rf-sputtering.
92. Ros, C., T. Andreu, and J.R. Morante, *Photoelectrochemical water splitting: a road from stable metal oxides to protected thin film solar cells.* Journal of Materials Chemistry A, 2020. **8**(21): p. 10625-10669.
93. McCafferty, E., *Thermodynamics of Corrosion: Pourbaix Diagrams*, in *Introduction to Corrosion Science*. 2010, Springer New York: New York, NY. p. 95-117.
94. Fountaine, K.T., H.J. Lewerenz, and H.A. Atwater, *Efficiency limits for photoelectrochemical water-splitting.* Nature Communications, 2016. **7**(1): p. 13706.
95. Guo, B., et al., *Facile Integration between Si and Catalyst for High-Performance Photoanodes by a Multifunctional Bridging Layer.* Nano Letters, 2018. **18**.